Montanuniversität Leoben / University of Wollongong

Phase Transformations and Grain Growth in TNM Based Alloys

Diploma Thesis

Thomas Klein

Leoben, October 2013

This thesis has been conducted at the Engineering Materials Institute, Department of Materials Engineering at the University of Wollongong, Australia, and submitted at the Chair of Physical Metallurgy and Metallic Materials, Montanuniversität Leoben, Austria. The thesis has been performed under the supervision of Prof. Dr. Rian Dippenaar, University of Wollongong, and Ass.Prof. Dr. Svea Mayer and Univ.-Prof. Dr. Helmut Clemens, Montanuniversität Leoben.

Eidesstattliche Erklärung

Ich erkläre an Eides statt, dass ich diese Arbeit selbständig verfasst, andere als die angegebenen Quellen und Hilfsmittel nicht benutzt und mich auch sonst keiner unerlaubten Hilfsmittel bedient habe.

Affidavit

I declare in lieu of oath, that I wrote this thesis and performed the associated research myself, using only the literature cited in this volume.

(Datum)   (Thomas Klein)

ACKNOWLEDGEMENTS

Many thanks to Prof. Dr. Rian Dippenaar, who initiated the partnership between the University of Wollongong and the Montanuniverstiät Leoben! Through this partnership it was possible to investigate materials from Austria on facilities in Australia. I gained many new and valuable perceptions through this experience. During my thesis Prof. Dippenaar's doors were always open for many fruitful discussions.

Furthermore I would like to thank all members of the Materials Process Engineering Group for their professional guidance on the local facilities. Special thanks to Dr. Salar Niknafs and DDr. Mark Reid for their assistance and their advice on different procedures and techniques.

I would like to express my gratitude to my supervisors Ass.Prof. Dr. Svea Mayer and Univ.-Prof. Dr. Helmut Clemens for their commitment and their encouragement, which made this project viable. Their support and motivation to supervise a joint intercontinental thesis rendered this project accomplishable. During my stay abroad I continuously received guidance through numerous video conferences and e-mails. Hereby I gained insight into an exciting field of science and an interesting class of material.

Furthermore I would like to thank my parents and my sister for their support during my years of study and during the period of my thesis. Early encouragement to engineering and science contributed to my motivation and a successful finishing of my studies.

Most importantly I would like to thank my fiancée Andrea for her commitment and persistence – priceless qualities to render a term abroad possible. Additionally I would like to thank her for her help and support during the time of the thesis and during our stay in Australia. We made the best of it!

ABSTRACT

Titanium aluminides represent an attractive option to replace Ni-base superalloys in various components of aero and automotive engines. Major reasons are a low density, good mechanical properties at elevated temperatures, good oxidation resistance and resistance against 'titanium fire'. The alloys under investigation were the TNM alloy containing the alloying elements niobium, molybdenum and boron as well as special TNM alloys which additionally contain carbon.

Aim of this study was to investigate phase transformations and grain growth *in-situ* in a high temperature laser scanning confocal microscope.

The β → α phase transformation was investigated regarding the morphology of the precipitating phase under different cooling rates. Low cooling rates yielded equiaxed structures, whereas high cooling rates yielded lath-like Widmanstätten structures. From the captured data continuous cooling transformation diagrams for the onset of β → α phase transformation were derived.

On annealing a carbon containing TNM alloy at high temperatures precipitation of second phase particles occurred. These precipitates were identified as Ti_2AlC carbides. An orientation relationship of these carbides and the γ-phase was observed.

Alloying effects on the formation of the γ-phase were studied. It was shown that carbon slows down the transformation process. Additionally, the occurrence of a cellular reaction in quenched and annealed samples was studied in the TNM alloy.

Grain boundary motion was investigated at a temperature of 1300°C. It could be shown that boundary migration in alloys containing a single phase field region at this temperature follows a parabolic kinetic law. Grain boundary motion in alloys containing a two phase field region is comparably slow and follows a linear law.

Additionally, grain growth was studied in the β single phase field region in β-solidifying alloys. The classic TNM alloy showed a smaller coarsening rate than the carbon containing TNM alloy as the β single phase field region is shifted to higher temperatures by alloying with carbon.

KURZFASSUNG

Titanaluminide stellen eine attraktive Möglichkeit dar, um Ni-basis-Superlegierungen in verschiedenen Komponenten von Flugtriebwerken und Automobilmotoren zu ersetzen. Die Hauptgründe dafür sind eine geringe Dichte, gute mechanische Eigenschaften bei erhöhten Temperaturen, gute Oxidationsbeständigkeit und Resistenz gegenüber ‚Titanfeuer'. Untersuchte Legierungen waren die TNM Legierung, welche die Legierungselemente Niob, Molybdän und Bor enthält, sowie spezielle TNM Legierungen, welche zusätzlich Kohlenstoff enthalten.

Ziel dieser Arbeit war es, Phasenumwandlungen und Kornwachstum in einem Hochtemperatur Konfokalen Laser-Scanning-Mikroskop *in-situ* zu untersuchen.

Die $\beta \rightarrow \alpha$ Phasenumwandlung wurde bezüglich Morphologie der gebildeten α-Phase unter verschiedenen Kühlraten untersucht. Niedrige Kühlraten führten zu äquiaxialen Strukturen, während hohe Kühlraten zu lanzettenähnlichen Widmanstätten Strukturen führten. Kontinuierliche Zeit-Temperatur-Umwandlungsschaubilder für den Beginn der $\beta \rightarrow \alpha$ Phasenumwandlung wurden erstellt.

Während der Auslagerung bei hohen Temperaturen wurde die Ausscheidung einer Zweitphase in einer kohlenstoffhaltigen TNM Legierung beobachtet. Diese Ausscheidungen wurden als Ti_2AlC Karbide identifiziert. Zwischen den Karbiden und der γ-Phase wurde eine Orientierungsbeziehung festgestellt.

Des Weiteren wurde der Einfluss von Legierungselementen auf die Bildung der γ-Phase untersucht. Es konnte gezeigt werden, dass Kohlenstoff den Umwandlungsprozess verlangsamt. Zusätzlich wurde das Auftreten einer zellularen Reaktion in der TNM Legierung an abgeschreckten und ausgelagerten Proben untersucht.

Die Wanderung von Korngrenzen wurde bei einer Temperatur von 1300°C untersucht. Dabei konnte gezeigt werden, dass die Verschiebung von Korngrenzen in Legierungen mit einem Einphasenfeld bei dieser Temperatur einem parabolischen kinetischen Gesetz folgt. Die Wanderung von Korngrenzen in Legierungen, welche ein Zweiphasenfeld enthalten, ist vergleichsweise langsam und folgt einem linearen Gesetz.

Weiters wurde das Kornwachstum im β Einphasenfeld in β-erstarrenden Legierungen untersucht. Die klassische TNM Legierung zeigte eine kleinere Vergröberungsrate als die mit Kohlenstoff legierte TNM Legierung, da das β Einphasenfeld durch das Legieren mit Kohlenstoff zu höheren Temperaturen verschoben wird.

TABLE OF CONTENTS

ABBRIVIATONS AND SYMBOLS

%	percent
®	registered trademark
°	degrees
°C	degree Celsius
°C/s	degree Celsius per second
µm	micrometer
A2	crystal structure of disordered β-phase
A3	crystal structure of disordered α-phase
Al	aluminium
Al_2O_3	aluminium oxide
at%	atomic percent
B	boron
B2	crystal structure of ordered $β_0$-phase
BSE	back scattered electrons
C	carbon
c/a	ratio of the c-axis to the a-axis
CCT	continuous cooling transformation
CO_2	carbon dioxide
$D0_{19}$	crystal structure of ordered $α_2$-phase
DSC	differential scanning calorimetry
EBSD	electron backscatter diffraction
FEG-SEM	field emission gun - scanning electron microscopy
G	Gibbs free energy
h	hours
He-Ne	helium-neon
HEXRD	high energy X-ray diffraction
HIP	hot isostatic pressing
H-phase	carbide of hexagonal structure
HTLSCM	high temperature laser scanning confocal microscopy
K	constant
kV	kilovolts
kW	kilowatt
$k_{βα}$	partition coefficient
L	liquid
$L1_0$	crystal structure of ordered γ-phase
LSCM	laser scanning confocal microscopy
mA	milli ampere

mbar	millibar
min	minutes
mm	millimeter
mm/s	millimeter per second
Mo	molybdenum
MoSi$_2$	molybdenum disilicide
MPa	megapascal
n	grain growth exponent
N	newton
Nb	niobium
nm	nanometer
NO$_x$	nitric oxide
OPS	suspension of colloidal silica
OR	orientation relationship
P-phase	carbide of perovskite structure
ppm	parts per million
Pt	platinum
R	correlation coefficient
r	radius
RF	reaction front
R$_M$	mean grain radius
rpm	revolutions per minute
s	seconds
SCR	silicon-controlled rectifier
SEM	scanning electron microscopy
t	time
T'	cooling rate
t$_1$	annealing time in the β single phase field region
T$_1$	temperature of β single phase microstructure
t$_2$	annealing time in the α+β phase field region
T$_2$	temperature in the α+β phase field region
T$_A$	annealing temperature
t$_A$	annealing time
T$_C$	temperature of the sample center
T$_{onset}$	temperature of the sample center
TEM	transmission electron microscopy
Ti	titanium
Ti$_2$AlC	chemical composition of H-phase
Ti$_3$AlC	chemical composition of P-phase

TiAl	titanium aluminide
TiB	titanium boride
TiB$_2$	titanium diboride
TN1.5Mo0.5C	TNM$^+$ alloy (TNM + 0.5Mo + 0.5C)
TNM	TiAl alloy of nominal composition Ti-43.5Al-4Nb-1Mo-0.1B
TNM$^+$	derivatives of the TNM alloy
TNM0.5C	TNM$^+$ alloy (TNM + 0.5C)
T$_\beta$	β-transus temperature
™	trademark
VAR	vacuum-arc-remelting
VIM	vacuum-induction-melting
wt%	weight percent
α	disordered hexagonal phase in TiAl alloys
α$_2$	ordered hexagonal phase in TiAl alloys
β	disordered cubic phase in TiAl alloys
β$_0$	ordered cubic phase in TiAl alloys
γ	ordered tetragonal phase in TiAl alloys
γ$_G$	γ-phase of globular morphology
γ$_{lamellar}$	γ-phase of lamellar morphology
Δt	cooling time

1 INTRODUCTION

Titanium aluminides have attracted attention in the automotive and aircraft industries due to their potential as light-weight structures in high temperature applications. A major justification for the development of advanced structural materials is the increasing global ecological awareness. In particular, a significant reduction of the pollutants CO_2 and NO_x is required, because of their severe impact on the quality of the atmosphere and the environment [1,2]. Thus, higher efficiencies in terms of fuel consumption in both automotive and aircraft industries are essential.

TNM™ alloys represent a subclass of complex multiphase γ-TiAl based alloys of the 3rd generation, which contain a balanced amount of β-stabilizers. In order to acknowledge the role of the major alloying elements, Nb and Mo, this γ-TiAl based alloy class has been named 'TNM alloys' [3]. The density of the TNM alloys is only about half the density of conventional materials for high temperature applications, such as steel and nickel-base superalloys [4]. This low density is a feature that makes them especially suitable for applications, such as turbine blades, valves or turbocharger wheels, which are all subject to highly dynamic loads. This significant weight reduction will in turn lead to a reduced moment of inertia and hence, reduced fuel consumption. For example, the replacement of nickel-base superalloy parts by γ-TiAl is expected to reduce the mass of gas turbine engines by 20-30% [2]. This will render the desirable decrease in fuel consumption and hence, a reduction of pollutants.

TNM alloys consist mainly of γ-phase, $α_2$-phase and small amounts of $β_0$-phase. These three phases display ordered intermetallic character at room temperature [5]. The inherently brittle nature of intermetallic compounds leads to problems with conventional shaping processes. Thus, advanced manufacturing techniques are required in order to enable economically viable production of TNM alloys and components.

With the intention to increase the temperature range of usage, further alloy development is required. Derivatives of the TNM alloy are generally termed TNM[+] alloys. Improved mechanical properties at elevated temperatures can be achieved by alloying with carbon to achieve solid solution hardening or precipitation hardening [1,6,7].

Material properties of TNM alloys are highly dependent on microstructural features such as colony size, the ratio of lamellae to globular grains as well as lamellar dimensions and spacing [8]. Enhanced microstructural control is therefore required. This can be achieved by a crucial selection of thermo-mechanical processing and heat treatment and hence, a fundamental understanding of the microstructural evolution is required to design the appropriate control measures. Two major high

temperature processes that influence the microstructural evolution are firstly solid-state phase transformations and secondly grain growth. Solid-state phase transformations can be positively exploited in order to achieve grain refinement, but the details of how exactly to achieve this are not yet fully understood [9]. Grain growth has to be controlled, because of its deleterious effects during processing on subsequent service properties.

The aim of the first part of this thesis is to contribute to the fundamental understanding of important solid-state transformations in γ-TiAl based alloys, namely the formation of the α-phase and the γ-phase. The effects of different cooling rates and alloy compositions are investigated. For the formation of the α-phase continuous cooling transformation diagrams are derived in order to quantify the effect of applied cooling rates. In addition, the formation of carbides in carbon containing alloys at elevated temperatures is examined.

The aim of the second part of this thesis is the study of grain boundary migration and grain coarsening at the selected temperature of 1300°C and a microstructural regime (β single phase field region). Grain boundary migration is studied by measuring the displacement of grain boundary junctions with respect to time. Grain coarsening is examined by using two approaches, firstly classic stereological estimation and secondly determination of equivalent circle diameter.

Most of the experimental work reported in this thesis has been conducted by the use of high temperature laser scanning confocal microscopy (HTLSCM), which allows capturing *in-situ* image sequences of events occurring in real time. In HTLSCM samples are heated in an infrared furnace. At the same time the surface is visualized by scanning a laser beam across the surface. Microstructural features are visible due to thermal grooving between grains and phases, thereby permitting *in-situ* observations at high temperatures and in real time. Optically clear images can be obtained up to a maximum operating temperature of 1750°C (for the facility in use) [10]. Additionally, *ex-situ* experiments have been carried out using field emission gun - scanning electron microscopy (FEG-SEM).
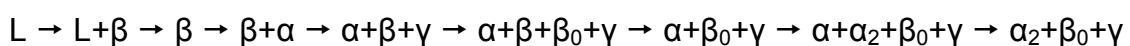
2 FUNDAMENTALS

In this chapter the theoretical foundations of the TNM alloying system and its derivatives are described. The first subchapter introduces the TNM alloying system with special emphasis on the role of phase transformations. In the second subchapter the fundamentals underpinning enhanced alloys are addressed.

2.1 TNM alloying system

TNM alloys are TiAl alloys based on the intermetallic γ-phase. The nominal composition ranges between Ti-(42-45)Al-(3-5)Nb-(0.1-2)Mo-(0.1-1)B (atomic percent (at%)) [11]. All chemical compositions in this thesis are given in atomic percent, unless otherwise indicated. The name TNM derives from the major alloying elements (Ti(Al)-Nb-Mo) of the material [3]. Within this work the alloy of nominal composition Ti-43.5Al-4Nb-1Mo-0.1B will be referred to as TNM alloy. TNM alloys have low density, a high specific yield strength, a high specific stiffness, good oxidation resistance, resistance against 'titanium fire' and good creep properties at elevated temperature [1]. Due to these characteristics TNM alloys are favoured as a potential replacement of the twice as heavy nickel-base superalloys. In TNM alloys a spectrum of different mechanical properties can be achieved by exploiting a multitude of phase transformations in combination with recrystallization processes. In addition, a variety of microstructures can be obtained through selected processing techniques.

2.1.1 Phase diagram and constituent phases

The equilibrium phase diagram in the composition range of TNM alloys is displayed in Fig. 2.1, which is a quasi-binary cut through the multicomponent system xTi-xAl-4Nb-1Mo-0.1B, where only the content of aluminium is varied. It is pertinent to assess the cooling sequence along the red vertical line, which shows that TNM alloys solidify via the β-phase in a temperature window of about 100°C. Many β-grains form at pre-existing borides, which are already present in the melt. Below the solidus temperature, the alloy exhibits a β single phase field region. During further cooling below the β-transus temperature α-phase is precipitated (details in subchapter 2.1.4.1) and thereafter below the α-transus temperature the γ-phase is precipitated (details in subchapter 2.1.4.3). In addition, the ordering of the α- and the β-phase into the α_2- and the β_0-phase occurs (details in subchapter 2.1.4.6). As shown in the equilibrium phase diagram, Fig. 2.1, five different phases can be present in the TNM alloy. Neglecting the presence of borides, the evolution of the phases on cooling the TNM alloy along the vertical line in the phase diagram can be summarized as follows:

$$L \rightarrow L+\beta \rightarrow \beta \rightarrow \beta+\alpha \rightarrow \alpha+\beta+\gamma \rightarrow \alpha+\beta+\beta_0+\gamma \rightarrow \alpha+\beta_0+\gamma \rightarrow \alpha+\alpha_2+\beta_0+\gamma \rightarrow \alpha_2+\beta_0+\gamma$$

L refers to liquid, whereas the other letters refer to the constituent phases, which will be described in more detail in the following paragraph.
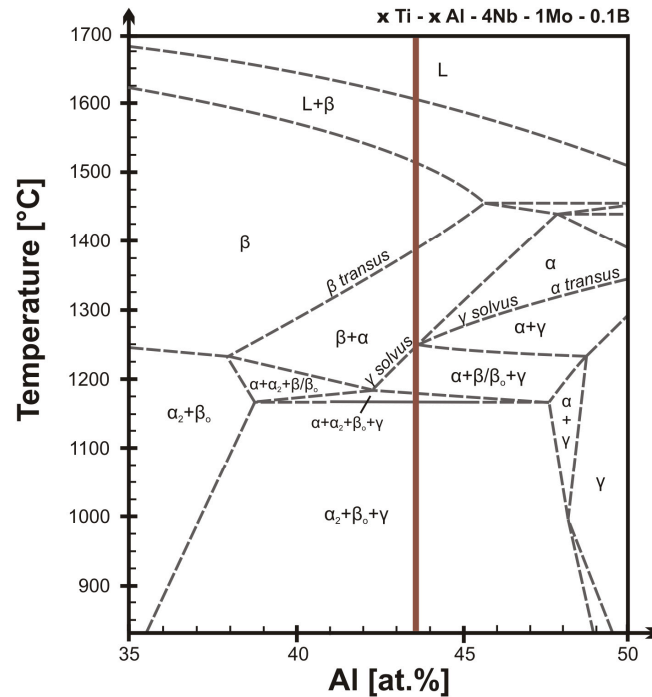
Fig. 2.1: Quasi-binary phase diagram of the TNM alloy [8]. The vertical line refers to the nominal composition of the TNM alloy under consideration.

The actual occurrence of a specific phase depends on the pertaining temperature, the exact composition of the alloy and the thermal history. Fig. 2.2 illustrates the crystal structures of the five phases, including the corresponding notation. Fig. 2.2a) and Fig. 2.2b) show the disordered phases A2 and A3, while Fig. 2.2c), Fig. 2.2d), and Fig. 2.2e) show the ordered phases B2, $D0_{19}$ and $L1_0$. In a) and b) white circles refer to titanium and aluminium, because of the solid solution character. In c), d) and e) black circles correspond to titanium and white circles correspond to aluminium, in order to emphasize the ordered intermetallic character.

Fig. 2.2: Crystal structures of phases in TNM alloys. a) β-phase, b) α-phase, c) $β_0$-phase, d) $α_2$-phase and e) γ-phase. After [12,13].

The disordered β-phase Fig. 2.2a), present at high temperature, is of engineering interest, because this high temperature phase supplies sufficient independent slip systems to allow for forging operations. Hence, it should always be present when hot working is performed [14,15]. On cooli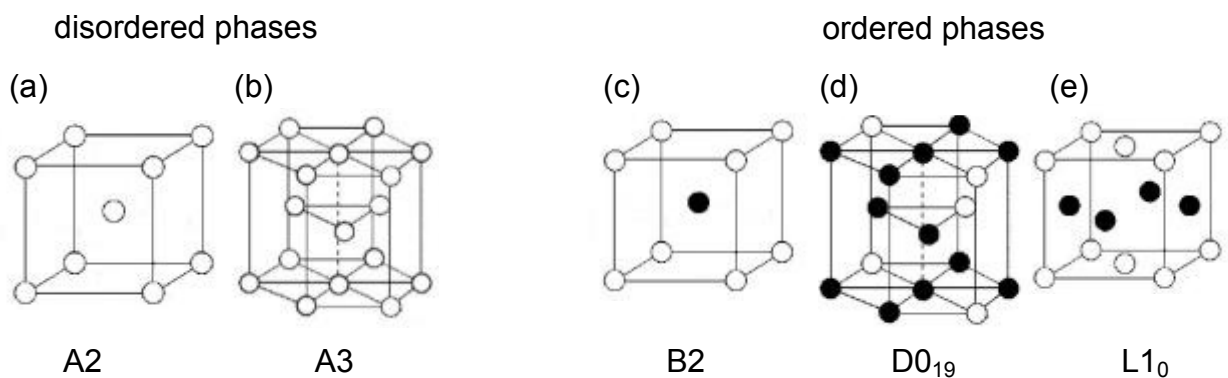ng, the disordered hexagonal α-phase Fig. 2.2b) forms. Due to the hexagonal crystal lattice this phase does not provide sufficient slip systems for uniform deformation. However, the β → α phase transformation offers the possibility of significant grain refinement. As the temperature is lowered further, the ordered γ-phase forms Fig. 2.2e), which is the major phase in TNM alloys. The β_0- and the α_2-phase (Fig. 2.2c) and d)) are the ordered counterparts of the β- and the α-phase. At room temperature TNM alloys consist of a large amount of γ-phase and smaller amounts of α_2-phase and β_0-phase. Through subsequent heat treatments the goal is to remove the β_0-phase, due to its negative effect on creep properties at service temperature. Additionally, the β_0-phase can decompose to harmful low ductile phases (low crystal symmetry) during service [16,17].

2.1.2 The role of alloying elements

Aluminium

With a nominal amount of 43.5at%, aluminium is the major alloying element in TNM alloys. It is a strong α-stabilizing element, indicated by the fact that the α-transus temperature rises with an increasing amount of aluminium. The α-transus temperature shows a large slope at amounts of about 43.5at% aluminium. This slope has to be small in order to render concentration deviations non-critically and this change in slope can be achieved through appropriate alloying. Additionally, the α single phase field region is expanded with increasing amounts of aluminium [1,4].

Niobium and Molybdenum

The refractory metals niobium and molybdenum are strong β-stabilizing elements, with molybdenum having a 3.9x stronger effect [3]. Molybdenum shows a higher partition coefficient $k_{\beta\alpha}$ [1]. The stabilization of the β-phase has an effect on the solidification pathway (non-peritectic), which shall be discussed in more detail in sub-chapter 2.1.3. Additionally, niobium leads to a higher eutectoid temperature. Enhanced ductility stems from niobium's influence on the stacking fault energy, which increases the likelihood for mechanical twinning. Moreover niobium modifies the structure of the surface oxide layer [3]. Both niobium and molybdenum diffuse slowly, resulting in a sluggish transformation behaviour of the β-phase, since these elements are mainly in solution in this phase [1,14]. This effect can be positively utilized as it leads to a more stable microstructure at forging temperatures, since the β-phase aligns along the α-phase grains, thereby reducing the rate of grain growth. However,

a negative effect is the slow dissolution of the β-phase during heat treatments, when the goal is the removal.

Niobium and molybdenum increase the oxidation resistance and the creep resistance. The oxidation resistance can limit the service temperature and time. The creep resistance also limits service temperature and time, as there are certain maximum elongations allowed depending on the field of usage [4].

Boron

The element boron is added in small amounts as a grain refining agent. Boron builds, mainly with titanium, thermally very stable borides of different chemical composition. These lead to a fine and homogeneous microstructure as they act as heterogeneous nucleation sites during solidification and during β → α phase transformation [9,18,19]. Additionally, borides slow the grain coarsening rate down during processes such as high-temperature heat treatments or welding [1].

2.1.3 β-solidification and the β single phase field region

A β-solidification pathway in comparison to a peritectic solidification pathway is desirable for several reasons. The microstructure following the β-solidification pathway is fine, texture-free and exhibits little segregation, whereas peritectic alloys are prone to forming coarse grains, solidification texture and strong segregation [20]. TiAl alloys have a high solubility of refractory metals that show a higher partition coefficient $k_{\beta\alpha}$ for the β-phase. A β-solidification pathway can be achieved by lowering the amount of α-stabilizing elements (Al, C) and alloying with β-stabilizing elements (Nb, Mo). A β-solidification pathway additionally provides the possibility of significant grain refinement by the use of the β → α solid-state phase transformation [9].

TNM alloys solidify primary via the β-phase [16]. The solidification pathway of L → L+β → β is schematically illustrated in Fig. 2.3. Above the liquidus temperature the alloy is completely molten. When cooling below this temperature a certain driving force acts to create lowest free energy in the system, which leads to the stability of solid phases. However, undercooling is necessary to build stable nuclei. The undercooling is required to create a sufficient driving force [21]. The applied undercooling influences the amount of nuclei as well as their growth rate. At low undercooling very few nuclei are able to overcome the energy for stable nucleation. At high undercooling the driving force is high, but slow diffusion limits the nucleation rate. Hence, the rate of stable nucleation exhibits a maximum with respect to the undercooling [21,22]. Nucleation from the melt can generally be divided into homogeneous and heterogeneous nucleation. The former refers to nucleation of solid particles directly from the melt, which is generally attributed to a high energy for nucleation, thus, a high required undercooling. The latter refers to nucleation on the surface of a third phase,

which is generally attributed to a lower energy consumption and a lower undercooling [21]. In TNM alloys heterogeneous nucleation occurs on the surface of the mould as well as on borides. Additionally, homogenious nucleation from the liquid is possible. The growth morphology of the β-phase from the liquid is dendritic [23].

At temperatures below the solidus temperature the alloy is completely solid. For a certain temperature interval, which depends on the exact alloy composition, a β single phase field region in the morphological form of large equiaxed grains is present. Alloys containing extended single phase field regions are prone to grain growth as they show a high grain boundary mobility [24]. *A displacement of a grain boundary is entirely equivalent to the growth on one crystallite at the expense of the shrinking neighbour [25].* Grain boundaries basically move through creation of lattice sites on the one side and corresponding destruction on the other side. The motion of grain boundaries is affected by interaction of the boundary with imperfections of the crystal. Such imperfections can be vacancies, dislocations, phase interfaces or external crystal surfaces [25].
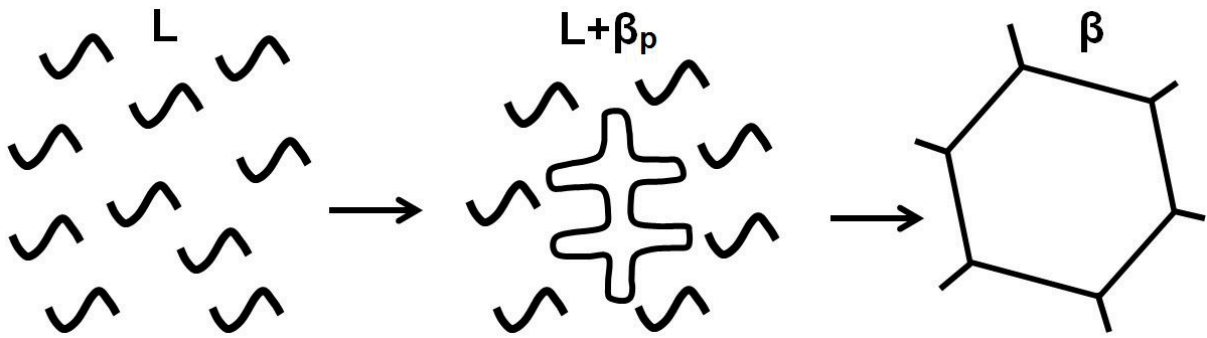
Fig. 2.3: Schematic β-solidification pathway of TNM alloys. Transformation sequence after [23].

Several laws have been developed to describe the evolution of grain size with respect to time at a certain temperature. One of the most common relationships developed by Burke and Turnbull [26] is given in Eq. 2.1, where R_M is the mean grain radius, K is a constant, which includes the grain boundary energy, t is the time and n is the grain growth exponent.

$$R_M^n = K \cdot t \qquad\qquad (2.1)$$

This relationship is based on several assumptions, such as that the forces acting on a grain boundary are only due to its curvature and the independence of the grain boundary energy on the grain radius. As this law derives from the displacement of single grain boundary it is valid for the mean grain radius as well as for the radius of individual grains [24].

2.1.4 Solid-state phase transformations

The study of phase transformations, as the name suggests, is concerned with how one or more phases in an alloy (the system) change into a new phase or mixture of phases [22].

The relative stability of a phase is frequently measured by the Gibbs free energy (G). However, whether a certain phase can actually be observed is dependent on the kinetics of the ongoing processes. In the case of diffusional phase transformations kinetic is strongly controlled by the atomic mobility, i.e. diffusion, which again is related to the state of thermal activation. At the phase interface of the growing phase a driving force acts to create the equilibrium composition [27]. However, in multi-component systems such as TNM alloys, it is not easily evident which element's diffusion is the rate controlling step [28]. In the following subchapters important solid-state phase transformations in TNM alloys will be described.

2.1.4.1 β → α phase transformation

Upon cooling from the β single phase field region, the disordered α-phase of hexagonal crystal lattice becomes thermodynamically stable. Three relevant energy terms are involved. Firstly a volume free energy reduction through the creation of the phase of lowest free energy, secondly the free energy increases due to the surface energy and thirdly the free energy increases due to the misfit strain energy that originates from the fact that the new phase does not ideally fit in the parental phase lattice [22].

The α-phase usually nucleates from grain boundaries, triple points and on borides if the alloy contains boron. The solid-state transformation sequence starting from the β single phase field region is schematically shown in Fig. 2.4. An orientation relationship, called the Burgers orientation relationship, between the β parental phase and the precipitating α-phase is observed. In terms of crystallography this orientation relationship is given by Eq. 2.2. The slip planes of the bcc lattice convert into the basal planes of the hexagonal lattice and the slip directions convert into the respective orientations and hence, 12 different orientations of the α-phase are possible [12,29].

$$\{0001\}_\alpha//\{110\}_\beta, \langle 1120 \rangle_\alpha//\langle 111 \rangle_\beta \tag{2.2}$$

Since nucleation occurs on many sites at the grain boundary of one β parental grain, a significant grain refining effect is achieved. However, subsequent α_2/γ-colonies are aligned only into directions given by the Burgers orientation relationship, which annihilates the effect of the previous grain refinement. A significantly finer and more homogeneous microstructure can be achieved in the presence of borides because the previous β-grains are already finer [9,18]. This effect is exploited in TNM alloys by small additions of boron.

It is known that the morphology of the α-phase is strongly dependent on the cooling rate [10]. High cooling rates favour fine Widmanstätten structures, while low cooling rates lead to equiaxed structures [9]. The shape of a growing second phase is determined by the relative migration rates of different crystal interfaces. Incoherent crystal interfaces are more mobile than semi-coherent or coherent interfaces. This fact leads to elongated structures if a growing second phase shows both types of interfaces. This qualitatively explains the origin of the morphology of Widmanstätten laths, which is a sharp and defined lath-like structure. Between these laths specific angles can be observed, which are related to the crystal structure. Planar phase interfaces are usually either coherent or semi-coherent [22].
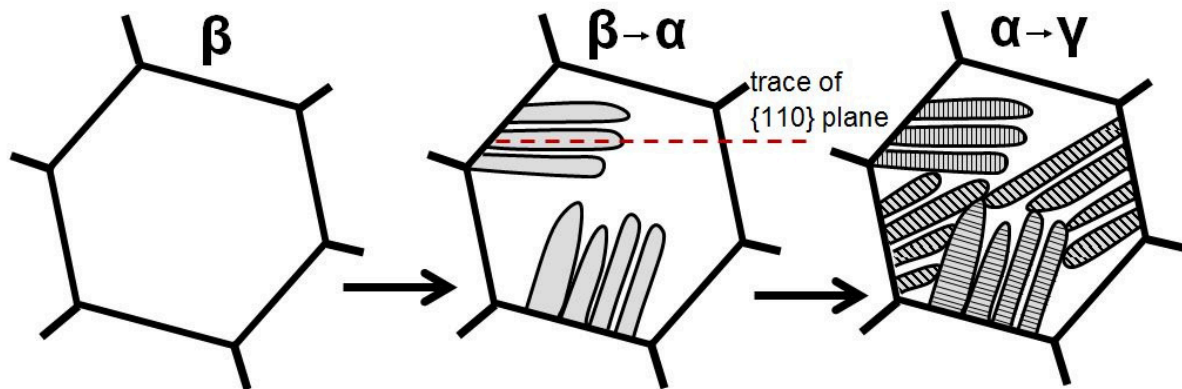

Fig. 2.4: Sequence of solid-state transformations in γ-TiAl based alloys. After [23].

2.1.4.2 The α+β phase field region

After formation of the α-phase two phases are present. This is useful, because hot-deformation processes take place at this temperature. A two phase microstructure is very stable and only minor grain coarsening occurs [14,16,30]. It has been shown that through annealing for long times a very small α single phase field region is present in TNM alloys of certain chemical composition [5]. However, a very small single phase field region is not of engineering significance, because it can be easily passed without significant coarsening effects on the microstructure.

2.1.4.3 γ-formation

The γ-phase constitutes the major phase in terms of phase fraction in TNM alloys. After cooling below the α-transus temperature the ordered γ-phase becomes thermodynamically stable. Hence, a thermodynamical force acts to create the lowest free energy in the system, which yields the onset of precipitation. The γ-phase starts to grow in the form of lamellae into the previous α-grains [23,31]. This reaction is a precipitation reaction and can be written as α → α+γ. The formation of the γ-phase is governed by the Blackburn orientation relationship, which is given in Eq. 2.3 [32].

$$(0001)_{\alpha_2}//\{111\}_\gamma, \langle 11\bar{2}0 \rangle_{\alpha_2}//\langle 1\bar{1}0] _\gamma \tag{2.3}$$

The close packed planes and directions are parallel to each other. As the {0001} plane of the α-phase does not show multiplicity, the precipitating γ-lamellae are also parallel to each other and perpendicular to the previous α-grains [33]. The resulting grains consisting of α_2/γ-lamellae are termed colonies [4,13]. The lamellar growth of the γ-phase is entirely diffusion controlled. A higher cooling rate leads to a finer evolving lamellar structure, due to limited diffusion.

The interface between α and γ is atomically flat over large distances. The basal planes of the α_2-phase and the {111} planes of the γ-phase lie parallel to each other. Besides these interfaces γ/γ interfaces are present. The lowest interfacial energies are provided by true twin boundaries, which are most frequently present. In the γ/γ interfaces coherency stresses and a large amount of misfit dislocations are present due to the slight variation from unity in the c/a ratio of the $L1_0$ structure [13].

Furthermore, a massive form of the γ-phase exists which is not controlled by diffusion [34]. Presently, there are no TiAl alloys in industrial use that utilize a massive γ-phase microstructure, but the massive microstructure can be used as a precursor to special lamellar microstructures [31]. Boron additions favour heterogeneous nucleation of lamellar γ-phase as opposed to the massive type of transformation as it is the case in TNM alloys [1].

At elevated temperatures the γ-lamellae change their shape into a globular structure following thickening of the lamellae in the α_2/γ-colonies. The driving forces for both effects are the minimisation of interfacial energy and the equilibration of the phase fractions through adjustment of the γ-phase fraction. At a critical thickness the γ-lamellae will change their shape into a globular form [35].

In addition, a lens-shaped γ-phase, which is the product of the solid-state transformation $\beta/\beta_0 \rightarrow \gamma$ is embedded around the colonies. This transformation is a result of the requirement to bring the phase fractions closer to equilibrium [5].

2.1.4.4 Precipitation of the γ-phase

At sufficiently high cooling rates from above the α-transus temperature, the formation of the γ-phase is supressed, typically when the cooling rate is higher than about 55°C/s. The room temperature microstructure then consists of highly supersaturated α_2- and β_0-phases. Large dimensions of a component yield different microstructures through the components thickness in rapidly cooled parts because the local cooling rates differ significantly [13]. The supersaturated microstructure is thermodynamically unstable and transforms through the precipitation of the γ-phase during subsequent ageing treatments if sufficient thermal activation is available. The driving force is equivalent to that described in subchapter 2.1.4.2 and in TNM alloys activation is achieved at approximately 700°C - 720°C [14,36]. At low ageing temperatures the precipitates formed are very fine due to a reduced diffusivity. The precipitation of

nm-scaled lamellar structures is described in detail in reference [37]. The precipitation of fine γ-lamellae is associated with an increase in strength and creep resistance. This can be explained by a modified Hall-Petch law, because the different interfaces act as obstacles for dislocations [37]. However, decreasing interlamellar spacing leads to a decrease in ductility [14,36].

2.1.4.5 Cellular reaction

A cellular reaction occurs in TiAl alloys in quenched and aged samples simultaneously with the precipitation of fine γ-lamellae as described in subchapter 2.1.4.4. The cellular reaction is a discontinuous solid-state moving boundary reaction. It is characterized by an abrupt change in orientation between matrix and product phase. The reaction product aggregates in such a way that a short path of diffusion is realized [38]. This process is schematically shown in Fig. 2.5. In TNM alloys the cellular reaction follows the path of $(\alpha_2+\gamma)_{fine} \rightarrow (\alpha_2+\beta_0+\gamma)_{coarse}$ (summarized). The reaction starts at colony boundaries, because both nucleation and diffusion is favoured in this region. Driving forces are the minimisation of the interfacial energy and the redistribution of phases and the adjustment of phase fractions in order to attain an equilibrium state. The occurrence of the cellular reaction in TNM alloys yields low strength and hardness in comparison to a heat treatment that leads to fine lamellar structures [39]. However, the plastic fracture strain is significantly increased, which is attributed to microstructural refinement [36,39]. The cellular reaction in TNM alloys is described in detail in reference [39].
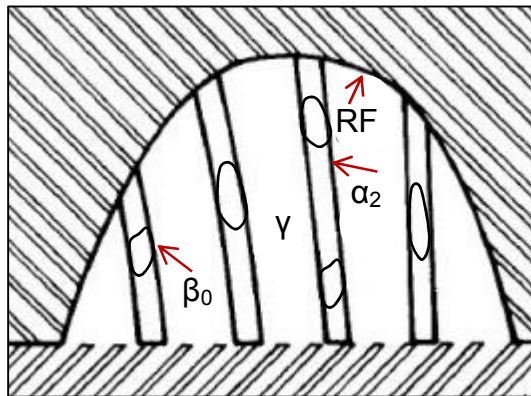
Fig. 2.5: Schematic illustration of a cellular reaction. RF is the reaction front; α_2, β_0 and γ correspond to the phases involved. After [38].

2.1.4.6 Ordering transformations

In solid solutions with a strong negative enthalpy of mixing dissimilar neighbouring atoms are preferred to similar, being the creation for the formation of ordered phases. In these structures lattice sites are denoted as A and B according to the atom type

positioned on these sites. However, in practice some non-stoichiometric phases can form through either vacant lattice sites or atoms sitting on wrong sites [22].

Ordering transformations in TiAl alloys are relevant because of the mechanical properties of the present phases are changed during ordering [5]. Ordering reactions cannot be supressed by quenching due to the very short diffusion pathways. The driving force for ordering is the minimisation of free energy in the system after a temperature drop below the respective transformation temperature. The microstructure of TNM alloys is based on a majority of γ-phase as stated above. This phase is found to be thermodynamically stable at temperatures lower than the α-transus temperature, which is reported to be about 1286°C in the TNM alloy [5]. The γ-phase does not have a disordered counterpart but decomposes during heating. The α_2- and the β_0-phases are the ordered counterparts of the high temperature phases α and β. In the TNM alloy the β-phase orders at about 1225°C [5]. The ordering reaction of the α-phase takes place at the eutectoid temperature. The ordering temperature of the α-phase in the TNM alloy is about 1174°C [5]. The ordering reactions are associated with changes in solubility as evident from the phase diagram shown in Fig. 2.1. If the temperature is lowered below the ordering temperature of the α-phase, the aluminium content is too large to build the α_2-phase of equilibrium composition (supersaturation). This leads to two reactions, $\alpha_2 \rightarrow \gamma_{lamellar}$ and $\beta_0 \rightarrow \gamma_G$. The first reaction yields the formation of additional γ-phase of a lamellar morphology. The second reaction leads to the formation of γ-phase of a globular morphology, as the β_0-phase cannot take up the additional amount of aluminium. This reaction yields lens-shaped precipitates of the γ-phase mainly at the colony boundaries as previously described in subchapter 2.1.4.2 [40].

2.2 Novel alloys – the enhancement of TNM alloys

In order to increase the temperature field of usage for TNM alloys, new alloying elements and microstructures are being investigated. These derivatives of the TNM alloy are generally termed TNM$^+$ alloys. Different hardening effects such as solid solution and precipitation hardening are currently under investigation [6,7].

2.2.1 Alloying with carbon

A major part of the development concentrates to hardening effects of carbon in TNM alloys. Carbon is reported to increase creep strength and hardness at elevated temperatures [1]. Carbon can either be present in solid solution or in the form of different carbides, depending on the solubility limit of the constituent phases and the thermal history [6,7]. Following rapid cooling carbon will be present in solid solution. If thereafter an ageing treatment is performed, fine carbides are precipitated. In the

following paragraphs a brief introduction is given of the properties associated with carbon as an alloying element in TiAl alloys.

2.2.1.1 The peritectic solidification

Carbon is a strong α-stabilizing element, which shifts the phase boundaries in the equilibrium phase diagram in favour of the α-phase. The addition of more than 0.5at% of carbon leads to the peritectic solidification pathway. Additionally, the peritectic solidification is favoured in the presence of larger amounts of aluminium and if smaller amounts of niobium and molybdenum are present (in comparison to the TNM alloy). The reaction sequence of the peritectic solidification can be written as L → L+β → α [1]. Thus, the primary solidification is via the β-phase followed by the growth of the α-phase into the liquid and into the β-phase. Firstly, this growth sequence implies that the β → α phase transformation cannot be exploited for grain refinement as it is the case for β-solidifying alloys. Secondly, no temperature regime with a significant amount of β-phase exists in the solid-state. Thus, peritectic alloys are generally less suitable for forging operations.

The peritectic reaction is associated with large columnar grains, strong segregation and texture within the γ-phase [23]. This is because the peritectic reaction usually is not in equilibrium due to slow solid-state diffusion. Hence, equilibrium concentrations of the constituent phases cannot be achieved in the core of previously formed β-grains.

Carbon additionally shifts the eutectoid temperature to higher temperatures, but does not influence the α-transus temperature [1].

2.2.1.2 The α single phase field region

One of the advantages of the TNM alloy is the negligible α single phase field region that only occurs in alloys of certain chemical composition after very long annealing times (longer than 1h) due to the sluggish dissolution of the β-phase [5]. Through the addition of carbon the α single phase field region is widened, as carbon is a strong α-stabilizing element and all phase boundaries of the equilibrium phase diagram are shifted towards the aluminium rich side. The occurrence of this phase field region renders several disadvantages. One disadvantage is that heat treatments in this temperature regime lead to significant grain coarsening [20]. A second disadvantage is that only the presence of a sufficient amount of β-phase renders the material forgeable [14].

2.2.1.3 Carbon in solid solution and carbide formation

In TiAl alloys carbon is either present in solid solution or as precipitates. Both is associated with an increase of strength and a decrease in ductility [1]. The solubility limit for carbon (or general interstitial elements) of the constituent phases is

increased by alloying with refractory metals [6]. When carbon is present in solid solution it is generally uniformly distributed with carbon enrichments at dislocation cores (Cottrell clouds) [6]. The presence of carbon reduces the interlamellar spacing within the α_2/γ-colonies, since carbon increases the number of heterogeneous nucleation sites [1].

Two different types of ternary carbide structures are reported to form in Ti-Al-C alloys [7]. These two are of perovskite (P) Ti_3AlC structure or of hexagonal (H) Ti_2AlC structure and both carbides exist in a carbon-deficient form with respect to the crystal structure formula. [41]. P-phases generally precipitate at lower temperatures than H-phases [7]. Precipitation hardening in a controlled way is only possible by the utilization of the P-phase, because effective hardening requires the presence of small and densely spaced particles. H-phase is found to precipitate in the form of coarse elongated precipitates, which preferentially form non-homogeneously at dislocations [41]. In Fig. 2.6 the crystal structures of the P-phase and the H-phase are displayed. Light grey circle correspond to aluminium atoms, black circles correspond to carbon atoms and white circles correspond to titanium atoms. Both types of carbides have an orientation relationship with the γ-phase, as given by Eq. 2.4 and Eq. 2.5 for the P-phase and the H-phase, respectively [42].

$$(001)_P//(001)_\gamma, [010]_P//[010]_\gamma \tag{2.4}$$

$$(0001)_H//(111)_\gamma, [11\overline{2}0]_H//[\overline{1}01]_\gamma \tag{2.5}$$
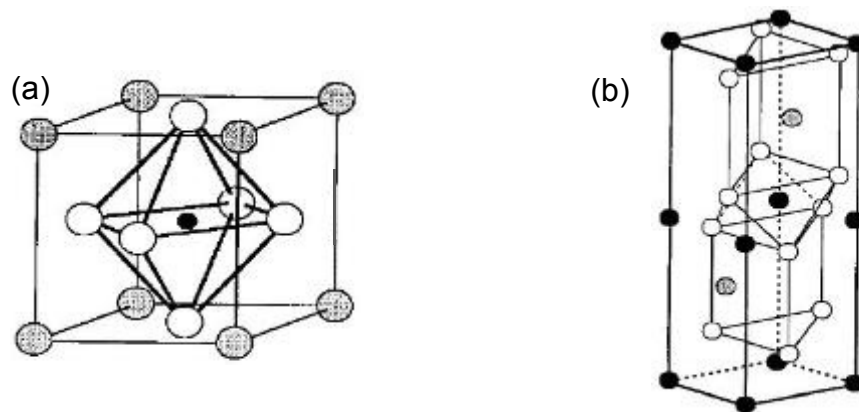

Fig. 2.6: Crystal structures of a) the P-phase and b) the H-phase [43].

2.2.2 β-compensated alloys

The disadvantages associated with carbon additions can be overcome by additional β-stabilization, for example by increasing the niobium and/or the molybdenum content. This has the effect that the solidification pathway is shifted back into

β-solidification. Hence, all negative effects due to peritectic solidification are avoided while the beneficial effects of carbon addition are retained.

2.3 Comparison of TNM and TNM⁺ phase fraction diagrams

For the *in-situ* study of the development of phases and phase transformations knowledge of phase fraction diagrams is of great value. For well-known systems these can be simulated by using thermodynamical databases. For the TNM alloy, the TNM0.5C alloy and the TN1.5Mo0.5C alloy the corresponding phase fraction diagrams were determined using high energy X-ray diffraction (HEXRD) [8,44]. Fig. 2.7 shows phase fraction diagrams for the alloys used for the current experiments of this study, but it is important to note that the temperature is differently scaled in each diagram.

Fig. 2.7a), Fig. 2.7b) and Fig. 2.7c) show the phase fraction diagrams of TNM, TNM0.5C and TN1.5Mo0.5C, respectively. In Fig. 2.7a) and Fig. 2.7c) the progress of precipitation of the α-phase (blue) from the β-phase (green) is visible. The phase fraction of the β-phase shows a minimum at about 1250°C for both alloys. Below the α-transus temperature the γ-phase (red) becomes thermodynamically stable and is thus formed. In Fig. 2.7b) the occurrence of an α single phase field region can be seen before the precipitation of the γ-phase occurs.
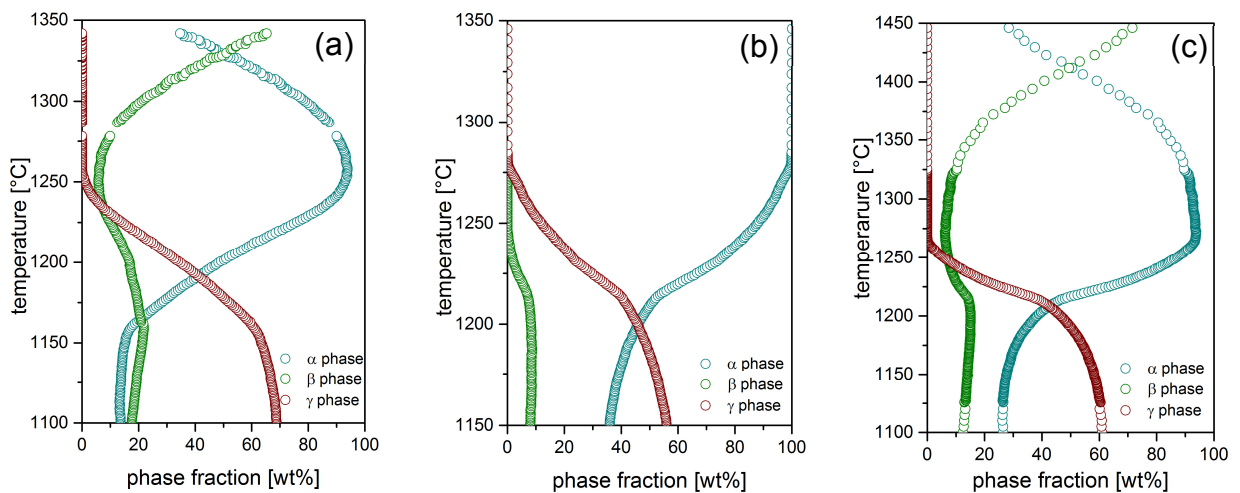

Fig. 2.7: Phase fraction diagrams as derived from HEXRD data for a) the TNM alloy, b) the TNM0.5C alloy and c) the TN1.5Mo0.5C alloy. After [8,44].

3 EXPERIMENTAL

This part of the thesis will deal with the fabrication method of the materials under consideration in this study and with the experimental techniques used. A general outline of how an experiment in a high temperature laser scanning confocal microscope (HTLSCM) is run will be drawn and details of the experimental parameters for each of the experiments will be provided. Parameters for *ex-situ* experiments on heat treated samples using field emission gun – scanning electron microscopy (FEG-SEM) will also be given.

3.1 Materials

The materials under investigation were produced using metallurgical melting by GfE Materials und Metals GmbH, Germany. The first material is the classic TNM alloy, referred to as TNM. The second material is additionally alloyed with 0.5at% carbon, referred to as TNM0.5C. The third material is alloyed with 0.5at% carbon and in addition the molybdenum amount is increased to 1.5at%, referred to as TN1.5Mo0.5C. Details about the alloying system are given in chapter 2. All the sample material was fabricated on industrial scale. A vacuum-arc-remelting (VAR) process was utilized in order to limit the amount of interstitial impurities (hydrogen, oxygen and nitrogen) and to gain chemical homogeneity. Products of the VAR process are cylindrical electrodes, which were subsequently melted using Vacuum-Induction-Melting (VIM) and thereafter cast using different casting methods. TNM and TN1.5Mo0.5C were cast using centrifugal casting; TNM0.5C was cast using gravity casting. Cylindrical bars with 55mm in diameter of TNM and TN1.5Mo0.5C and of 60mm in diameter of TNM0.5C were fabricated. These cylindrical bars were then hot-isostatically-pressed (HIP) in order to close the remaining porosity, which resulted from the casting process. The parameters of the treatment were as follows: a temperature of 1200°C for a time of 4h under a pressure of 200MPa and subsequent furnace cooling. In Table 3.1 processing details of each alloy are summarized and the chemical composition (actual and nominal) is given.

Table 3.1: Actual and nominal (in brackets) chemical compositions of the alloys and the pertaining fabrication processes.

alloy	lot #	VAR	casting process	chemical composition [at%]				
				Al	Nb	Mo	B	C
TNM	101519	2x	centrifugal casting	43.67 (43.5)	4.08 (4.0)	1.02 (1.0)	0.10 (0.1)	-
TNM0.5C	97043	1x	gravity casting	43.72 (43.5)	4.13 (4.0)	1.05 (1.0)	0.11 (0.1)	0.51 (0.5)
TN1.5Mo0.5C	114219-2	1x	centrifugal casting	42.95 (43.0)	4.09 (4.0)	1.53 (1.5)	0.11 (0.1)	0.48 (0.5)

3.2   High temperature laser scanning confocal microscopy

The basic technique of laser scanning confocal microscopy (LSCM) was patented by Minski in 1961 [45]. However, only in the 1990's interest was renewed, when a combination of the LSCM with an infrared heating furnace, termed high temperature laser scanning confocal microscopy (HTLSCM), was proposed in order to visualize metallic and ceramic materials *in-situ* at elevated temperatures up to 1750°C. The HTLSCM technique is typically used to study solidification phenomena, solid-state phase transformations, grain growth, particle coarsening, and dissolution of inclusions.

3.2.1 Experimental setup and imaging principle

In confocal microscopy a laser beam is focused onto the sample surface. The reflected beam is channelled into a photo detector. An image is generated by scanning the object relative to the focal point, which is stored for display by a computer equipped with an image capturing system. Contrast in a HTLSCM can be gained due to surface roughness. In the case of grain boundaries and phase boundaries surface roughening occurs via thermal etching. This effect is illustrated in Fig. 3.1. In this figure two neighbouring grains lying on the free surface are shown. Due to thermal activation of atom movement and resulting motion of individual atoms a groove is formed. Distinct angles between the grains are then governed by the relation of the interfacial energies [46]. As represented by the red arrows, light will be scattered and not reflected in the region of the groove. Hence, less light will reach the detector and the boundary can be identified because of its darker appearance. It has to be mentioned that every other effect causing surface roughness, e.g. different thermal expansion coefficients of different phases, also contributes to the image and might
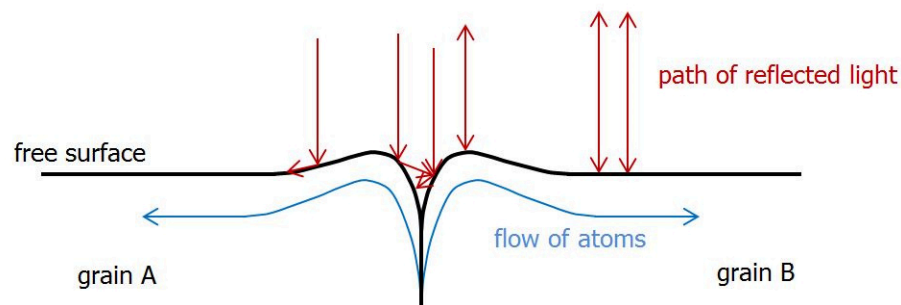
Fig. 3.1: Illustration of the effects of thermal etching. Red arrows indicate the reflected light, which is made visible in the HTLSCM.

mask the process of interest. As a consequence of the imaging principle the sample surface has to be polished to mirror image quality.

By using a confocal pinhole, only light from the focal plane is permitted to reach the detector, and a sharp image is produced. This alignment increases the resolution to an effective resolution of 0.25µm. Experiments performed with the HTLSCM are surface observations, however, bulk materials behaviour can be observed in many cases [47].

The experiments in this study were carried out on a confocal laser scanning microscope 1LM21H supplied by Lasertec Corporation, Japan. The maximum image capturing frame rate of this device is 30 images per second and a He-Ne laser with a wavelength of 632.8nm is used. The microscope is used in combination with an infrared furnace with a gold coated, high reflectivity, ellipsoidal cavity. A 1.5kW-halogen lamp is located at the lower focal point of the ellipsoidal cavity, while the specimen is located at the upper focal point. The sample and lamp chamber are separated by a quartz window, which allows a controlled atmosphere in the sample chamber. The halogen lamp can be air cooled. The setup of the furnace is illustrated in Fig. 3.2a) [47,48].

The sample is inserted into an yttria crucible of 8.5mm inner diameter. The thermodynamically very stable yttria crucible was chosen in order to reduce reaction of the sample material with the crucible material at elevated temperatures. Additionally, the crucibles were sintered at 1600°C for 12h, because it is known that less open porosity also reduces the reaction with the sample material. The crucible is thereafter inserted into a platinum holder equipped with a B-type thermocouple. Thermocouple and holder system are stabilized by an alumina tube. The position of the thermocouple requires a temperature calibration, which will be described in subchapter 3.2.5. The crucible holder system is illustrated in Fig. 3.2b). The temperature in the sample chamber is controlled by this thermocouple and the temperature is captured for subsequent evaluation.

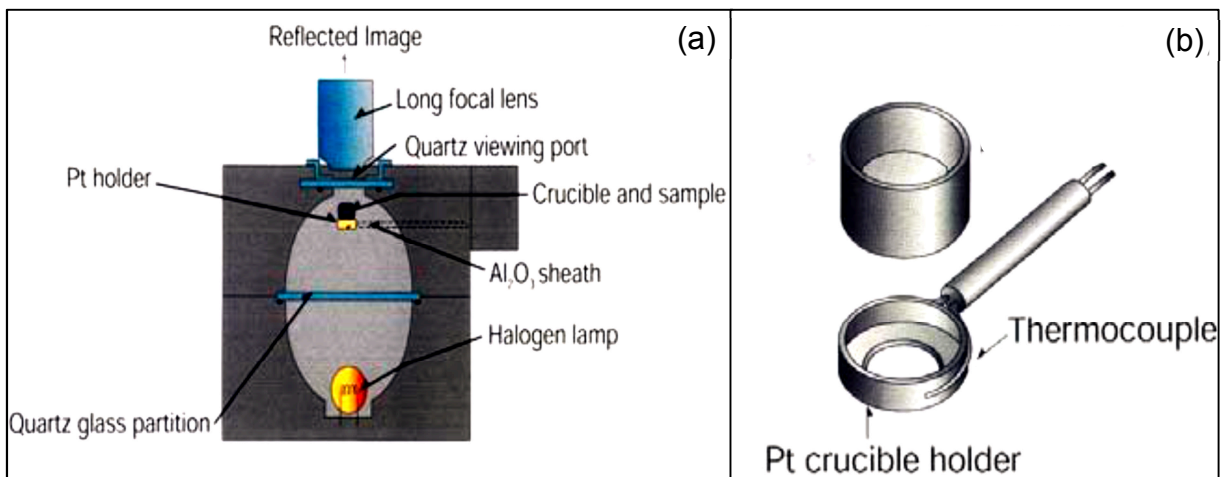Fig. 3.2: a) Schematic illustration of infrared furnace as used as heat source in an HTLSCM and b) crucible holder system. After [48].

3.2.2 Gas purification system

For the observation of highly reactive materials such as TiAl alloys, a high-integrity atmosphere with a very low oxygen concentration is necessary. Thin layers of oxide on the sample surface can make it impossible to generate an image.

High purity argon is used as atmosphere in the sample chamber. Additionally, the gas is cleaned with a purification train containing a furnace with a steel tube filled with zirconium shavings. The tube is inserted into a furnace in order to heat the zirconium to a temperature of 850°C. The argon gas stream passes the tube directly before it enters the sample chamber. Most of the remaining oxygen immediately reacts with the hot zirconium and is thus removed from the gas stream. Utilizing this technique an oxygen concentration of 10^{-15}-10^{-16}ppm can be achieved.

3.2.3 General experimental HTLSCM procedure

In this subchapter a short description will be given of how an experiment on the HTLSCM is run.

Firstly, the sample has to be cleaned with ethanol and is inserted into an yttria crucible. Both are then inserted into the platinum holder and put into the sample chamber. In the next step an image has to be generated by adjusting the evenness of the specimen relative to the angle of the beam. This step delicately influences the image quality that can be obtained.

Secondly, the sample chamber is flushed with argon. This procedure starts by closing the argon flow with a valve. At the same time a vacuum pump evacuates the sample chamber until a pressure of $2.2 \cdot 10^{-3}$mbar, is reached, which is followed by subsequent purging of the sample chamber with argon. Experimental experience has shown that a vacuum of this order applied 12 times in succession ensures that trace levels of oxygen are sufficiently removed to ensure that no oxidation takes place even at elevated temperatures and using reactive materials. In Fig. 3.3 the output data of the oxygen sensor of a typical purging sequence is plotted. Valleys correspond to pumping steps, whereas hills correspond to argon purging. The sharp peaks in between are due to backpressure of the system. It is apparent that the applied sequence of pumping steps lowers the oxygen content significantly.

Thirdly, the temperature profile is programmed in the control unit. Heating and cooling ramps over large temperature steps of a few hundred degrees are limited to a rate of 1.67°C/s in this system. Higher rates can lead to breakage of the alumina tube that contains the thermocouple, following thermal stresses. The program can be interrupted any time during the experiment or switched to manual control. This setting allows controlling the power input manually.

Fourthly, the image capturing system is switched on. As the last step before an experiment can be started, the cooling system is switched on.

During the experiment the magnification of the objective can be changed at any time. It is necessary to focus repeatedly onto the surface during the experiment because the holder system slightly moves the sample out of focus due to thermal expansion.

Focusing is performed manually by aligning the focal plane with the sample surface similar to the focusing procedure of a common light optical microscope.
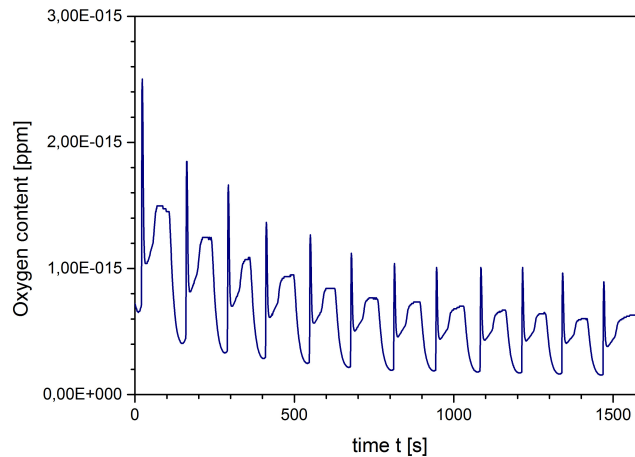

Fig. 3.3: Illustration of the argon purging sequence. Each valley corresponds to a pumping step, whereas each hill corresponds to flushing with argon. The sharp peaks are due to backpressure of the system.

3.2.3.1 Experimental procedure for the investigation of α-phase formation

In order to study the β → α phase transformation *in-situ* the following procedure was established for the visualisation of nucleation and growth of the α-phase. Additionally, the data gained from these experiments is utilized to derive continuous cooling transformation (CCT) diagrams.

Alloys TNM and TN1.5Mo0.5C were heated in the HTLSCM until a fully β-phase microstructure was established. The occurrence of a single β-grain microstructure is easy to distinguish, because only in single phase microstructures grain boundaries are strongly thermally etched. The knowledge of phase fraction diagrams for each alloy reveals that the single phase that forms must be the β-phase. Generally, the heating profile used can be illustrated as shown in Fig. 3.4. Temperatures and times illustrated in this figure can be found in Table 3.2 for each material. A magnification of
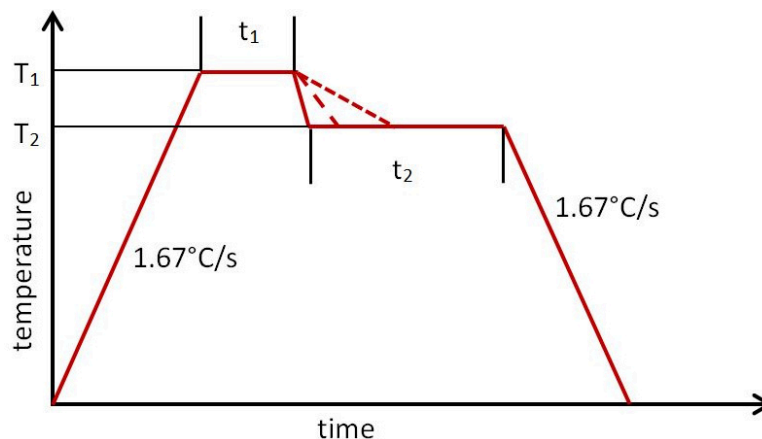

Fig. 3.4: Temperature profile as used for β → α phase transformation; T_1 and t_1 represent the parameters for the β-solution; T_2 and t_2 represent the holding temperature and the holding time.

180 was used. Different annealing times for the two different materials were necessary to gain a comparable initial microstructure of the β-phase.

Between T_1 and T_2 a continuous cooling rate was applied, which was varied between 0.03°C/s and 12.0°C/s (rates are given in Table 4.2, p.37 and p.38) to allow transformation to take place. Cooling was interrupted following a temperature drop of 80°C due to limitations of the microscope. This is a consequence of the impossibility of cooling over big temperature steps with high cooling rates. Thus the transformation into the α-phase is always incomplete, which is not considered to be problematic, since the TNM and the TN1.5Mo0.5C do not show an α single phase field region.

Table 3.2: Temperatures and times as illustrated in Fig. 3.4.

alloy	T_1 [°C]	t_1 [min]	T_2 [°C]	t_2 [min]
TNM	1405	5	1325	5
TN1.5Mo0.5C	1475	1	1395	5

3.2.3.2 Experimental procedure for the investigation of γ-phase formation

In this subchapter the experimental procedure to observe nucleation and growth of the γ-phase shall be described briefly.

The materials under observation were the TNM alloy, the TN1.5Mo0.5C alloy and the TNM0.5C alloy. A magnification of 340 was utilized to be able to resolve fine structures, such as α/γ-colonies during growth of the γ-phase. The temperature profile used can generally be represented as previously shown in Fig. 3.4. The temperatures and times of heat treatments were the same for all three alloys. After annealing for 10min at 1300°C the samples were cooled to 1150°C, where cooling was interrupted. The γ-phase is thermodynamically stable in all three alloys at this temperature. Hence, nucleation and growth of the γ-phase could be observed. Between these temperatures two different cooling rates of 12.5°C/s and of 1.67°C/s were applied.

3.2.3.3 Experimental procedure for the investigation of grain growth at 1300°C

Isothermal grain growth of the TNM alloy, the TN1.5Mo0.5C alloy and the TNM0.5C alloy at 1300°C was carried out using the parameters described below:

At 1300°C the TNM0.5C alloy exhibits an α single phase field region, whereas the TNM alloy and the TN1.5Mo0.5C alloy show an α+β phase field region. Therefore, significant differences regarding grain growth and grain boundary mobility are expected.

Samples of each alloy were heated to 1300°C and annealed for 20min. The chosen magnification was 340, because the effect of thermal etching is too weak to visualize grain boundaries in the TNM0.5C alloy at lower magnifications.

3.2.3.4 Experimental procedure for the investigation of grain growth in the β phase field region

TNM and TN1.5Mo0.5C alloys exhibit a β single phase field region. Aim of this sub-chapter is describe the experimental procedure used to investigate isothermal grain growth within this single phase field region *in-situ* in the HTLSCM.

The annealing temperature (T_A) and annealing time (t_A) were different for each alloy since the temperatures in the β single phase field region of equivalent microstructure are not the same. The chosen temperatures and times are given in Table 3.3. Annealing times differed significantly, because grain growth occurs at a far higher rate in the TN1.5Mo0.5C alloy than in the TNM alloy. At high temperatures grain boundaries are easily visible, because the effect of thermal etching is strong. This allows a low magnification of 85 which provides a wide area of observation and hence, a more reliable statistical assessment of the values of the grain size can be made.

Table 3.3: Temperature and times used for the study of grain growth in the β single phase field region; T_A and t_A are the annealing temperatures and times, respectively.

alloy	T_A [°C]	t_A [min]
TNM	1405	21
TN1.5Mo0.5C	1475	6.5

3.2.4 Sample preparation for the HTLSCM

Samples utilized in the HTLSCM have to be flat and the cutting planes have to be parallel. In order to gain high image quality a scratch free surface is required (see also subchapter 3.2.1).

Thin bars of 8mm diameter were eroded out of the raw bars. Disks of 1.4mm thickness were cut from these bars using a precision cutting apparatus Accutom-50, supplied by Struers, Germany, and a diamond cutting blade. Feed (0.02mm/s) and force (setting: low) were kept low to reduce the influence of heat generation on the initial microstructure.

Grinding and polishing procedure

Previously cut disks were hot mounted in Multifast resin using the hot mounting press CitoPress-20, both supplied by Struers, Germany. Thereafter they were manually ground using a sequence of silicon carbide abrasive paper, as given in Table 3.4, until no more scratches could be observed. After grinding manual polishing was performed using firstly a 6μm and secondly a 1μm diamond suspension. Before inserting the samples into the HTLSCM the mount was mechanically removed. The sample surface was covered with sticky tape in order to protect it. Then the mount was

manually cut with a saw so that the samples could be removed. Thereafter the samples were cleaned from remainders with ethanol.

Table 3.4: Sequence of abrasive paper used for the mechanical grinding procedure.

abrasive paper grade	P500	P800	P1200	P2400	P4000

3.2.5 Temperature calibration

Temperature calibration is necessary since the temperature is measured by a thermocouple that is positioned next to the crucible. A low-carbon steel sample (0.05wt% C) with known transformation temperatures was utilized for this purpose and the steel specimen was heated at a rate of 0.17°C/s. For calibration the nucleation temperature of δ-ferrite was used, since this transformation is in the temperature field of interest for the subsequent study and, moreover, this transformation is easily visible. The actual temperature was found to be 55°C higher than the output signal of the thermocouple. It has to be stated that this temperature calibration is only valid for the setup combination used in this study, which means the sample diameter and thickness, the crucible material and wall thickness, as well as the thermocouple used. One additional effect has to be taken into account when reliable temperature data is required. While the specimen is heated a thermal gradient is built up along the specimen radius, which is illustrated in Fig. 3.5. On the left side the top view of a sample is shown indicating the cutting plane for the section shown on the right hand
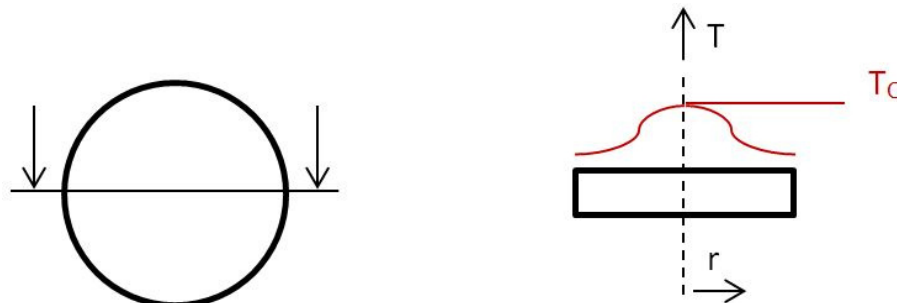

Fig. 3.5: Top view and section of a specimen to illustrate the built up thermal gradient alongside the radius.

side. On the right hand side the temperature profile is shown schematically with respect to the samples radius. The beam size of the heat source is approximately 2mm in diameter. Only within this region a well-defined temperature (T_c) is expected. Thus the sample centre was marked with an indent to ensure that all experiments were carried out within this field.

3.3 Field emission gun - scanning electron microscopy

Ex-situ experiments were carried out using a Field Emission Gun Scanning Electron Microscope JSM-7001F provided by Jeol Ltd., Japan. The EDX detector of type X-Max^N was supplied by Oxford Instruments, UK.

All images were taken in back scattered electron mode (BSE) at a voltage of 15kV and a current of 3.8mA. In BSE mode primary electrons are scattered by atom cores close to the sample surface. Contrast between the different phases is obtained by virtue of their different respective compositions. This technique can neither be utilized in common optical microscopy nor in the HTLSCM.

3.3.1 Sample preparation for the FEG-SEM

In order to provide good BSE contrast the samples have to be polished as flat as possible so that no shading effects can influence the image. As most of the samples were analysed after the heat treatment in the HTLSCM, the sample geometry was generally taken to be the same as for these experiments, i.e. 8mm in diameter and a thickness of 1.4mm. These disks were embedded in Multifast resin and thereafter manually ground with the sequence of abrasive paper given in Table 3.4. Thereafter the specimens were automatically polished using OPS suspension supplied by Struers, Germany. In this suspension colloidal silica (0.04µm) is used as the abrasive. In combination a chemical interaction occurs, which forms a brittle oxide layer that is continuously removed by the silica particles. Parameters of the OPS polishing step are given in Table 3.5.

Table 3.5: Parameters for the automatic OPS polishing step.

force [N]	time [s]	rotational direction	drive [rpm]	water
20	180	counter rotation	150	off

After polishing, the samples were carefully removed from the resin (as previously described) and glued onto an aluminium disk acting as a sample holder using copper sticky tape. By using this approach four samples can be placed in the FEG-SEM sample chamber at the same time and achievement of the required vacuum is faster than when a resin-based mount is utilized.

3.4 Furnace heat treatments

The annealing procedure was carried out on a laboratory scale on a high temperature vacuum tube furnace GSL-1600-80X supplied by MTI Corporation, USA. The furnace is equipped with $MoSi_2$ heating elements. The temperature is controlled by a silicon-controlled rectifier (SCR) power controlling unit. The furnace was used in air. For the determination of the temperature an R-type thermocouple was utilized. The position of the thermocouple in the furnace tube was marked so that thereafter the samples were positioned exactly at the same place where the temperature was measured. This is required due to the fact that the temperature varies along the axis of the furnace tube. Using this method the temperature is accurate to ±5°C. Disk shaped TNM samples of 8mm in diameter and a thickness of 1.6mm were used. After

the heat treatment about 0.6mm were mechanically removed from the sample surface in order to reduce the impact of the furnace atmosphere. This was proven by heating one sample in the HTLSCM to 1300°C. No serious oxidation occurred. Samples were inserted into the furnace, which was preheated to 1290°C (T_1), while special care was taken to open the furnace very quickly so that impact on the temperature was negligible. This is important in order to treat the samples in a reproducible manner. Samples were solution annealed at 1290°C for 10min (t_1) and thereafter quenched in water in order to supersaturate the α-phase at room temperature by supressing the formation of the γ-phase. The heat treatments used are summarized in Table 3.6. Parameters are displayed in the image next to the table. t_2 is the annealing time and T_2 is the corresponding annealing temperature.

Table 3.6: Times and temperatures of the performed heat treatment as displayed on the right.

sample	temperature T_2 [°C]	time t_2 [min]
#1	1150	15
#2	1150	75
#3	950	15
#4	950	75
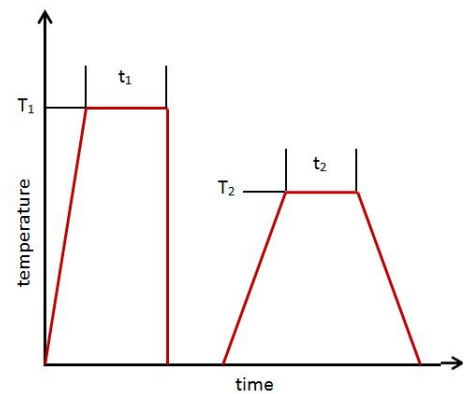
4 RESULTS AND DISCUSSION

This chapter is separated into two major parts. In the first part emphasis is placed on solid-state phase transformations occurring in γ-TiAl based alloys, whereas the second part deals with isothermal grain growth. Experiments in both parts are carried out on the TNM, the TNM0.5C and the TN1.5Mo0.5C alloys in order to investigate the influence alloy composition.

4.1 Initial microstructures

In order to make a reasonable comparison of the resulting microstructures after heat treatment, SEM micrographs of the cast and HIPed materials were made. These are displayed in Fig. 4.1. In these images the microstructure of a) the TNM alloy, b) the TNM0.5C alloy and c) the TN1.5Mo0.5C alloy are shown. The bright phase is the β_0-phase, the grey phase is the α_2-phase, and the dark phase is the γ-phase. In all images lamellar colonies of α_2/γ are visible. The γ-phase is also present in a globular/lens-shaped morphology (γ_G), mainly at the colony boundaries. In Fig. 4.1a) the constituent phases of the microstructure are labelled and indicated by red arrows. Fig. 4.1b) shows that the room temperature microstructure of the TNM0.5C appears
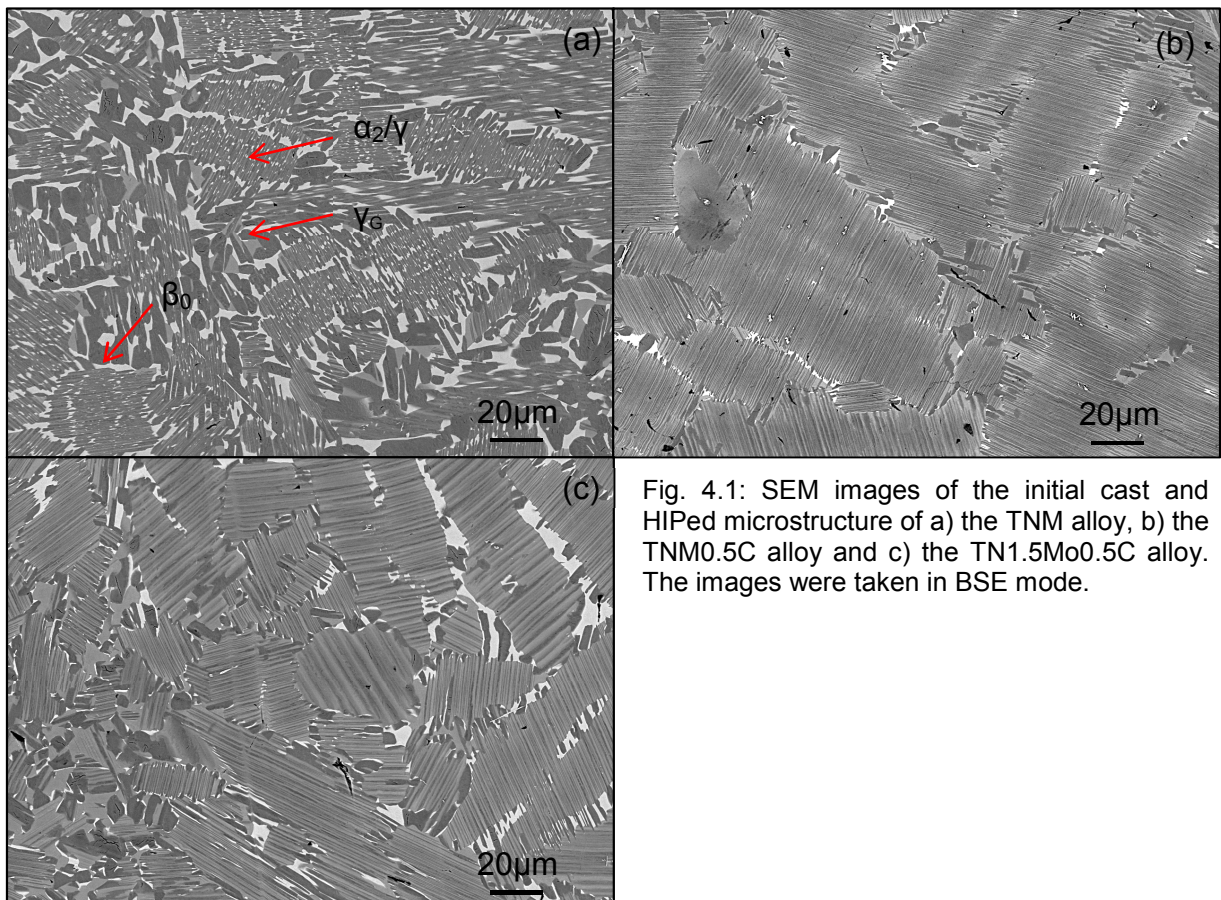

Fig. 4.1: SEM images of the initial cast and HIPed microstructure of a) the TNM alloy, b) the TNM0.5C alloy and c) the TN1.5Mo0.5C alloy. The images were taken in BSE mode.

to be very coarse, which is a direct result of the peritectic solidification pathway. In this alloy a smaller amount of β_0-phase is present at room temperature. Fig. 4.1c)

shows the room temperature microstructure of the TN1.5Mo0.5C alloy. Similarities to the microstructure of the TNM alloy are evident. However, a less homogeneous distribution of the constituent phases in various morphological features is observed.

Part I: Solid-state phase transformations

Phase transformations are of general interest because they strongly influence subsequent bulk material properties, especially mechanical properties. In order to control the microstructure, information of the microstructural evolution is necessary. Judicious manipulation of phase transformations can be used to obtain grain refinement by repetitive cycling through the transformation temperature or by controlling the size of precipitating phases by the exact manipulation of annealing temperatures and times. In order to utilize such transformations, a detailed knowledge of the influence of cooling rate and alloying element additions on the pertaining kinetics and morphology of the evolving phases is necessary. Hence, the aim of the following subchapters is to investigate the mechanisms of major phase transformations, specifically the formation of the α- and the γ-phases, in γ-TiAl based alloys.

4.2   Study of the $\beta \rightarrow \alpha$ phase transformation

The α-phase is one of the major phases in TiAl alloys. A significant amount of this phase is present at room temperature as the ordered α_2 counterpart, which strongly influences the mechanical properties. The $\beta \rightarrow \alpha$ phase transformation is employed industrially in order to refine the microstructure significantly and, in addition, the morphology of the precipitating α-phase can have an influence on the resulting mechanical properties. Furthermore it can affect the properties indirectly through its subsequent influence on the morphology of the γ-phase. The main goal of this subchapter is to elucidate the effect of cooling rate and alloy composition on the evolving α-phases morphology. This data is then used to construct continuous cooling transformation (CCT) diagrams. Furthermore the formation of H-carbides in carbon containing alloys at elevated temperatures is described.

4.2.1   Evolution of the α-phase

Visualising high temperature phase transformations *in-situ* is of great value to the design of the temperature profile of any casting process, as well as for subsequent heat treatment procedures. Hence, this subchapter will deal with the interpretation of image sequences gained from HTLSCM experiments by discussing observations made on a representative example.

In order to develop a procedure to study the evolution of the α-phase the beginning of the melting of the TNM alloy and the TN1.5Mo0.5C alloy were determined. These are about 1460°C and 1500°C, respectively.

In Fig. 4.2 an image sequence of the evolving α-phase in the TNM alloy is displayed while it is cooled at a rate of 0.08°C/s following a solution heat treatment at 1405°C for 300s. In the following any set of temperature and time for a solution heat treatment is referred to as solution temperature and solution time. The short time for the solution heat treatment is chosen because it is known that a large initial grain size promotes the formation of Widmanstätten structures [10]. In Fig. 4.2a) mostly β-phase is present at 1375°C, which was found to be the onset temperature of transformation at this cooling rate. The red arrow indicates a β-grain boundary, whereas the yellow arrow marks a thermal groove, which represents former grain boundaries of the α-phase, which do not vanish immediately after heating. This type of groove often crosses the β-grain boundaries, which proves that they are not small angle grain boundaries in the β-phase, but grooves of pre-existing grain boundaries. In Fig. 4.2b) growth of the α-phase is visible at many different sites, mainly from grain
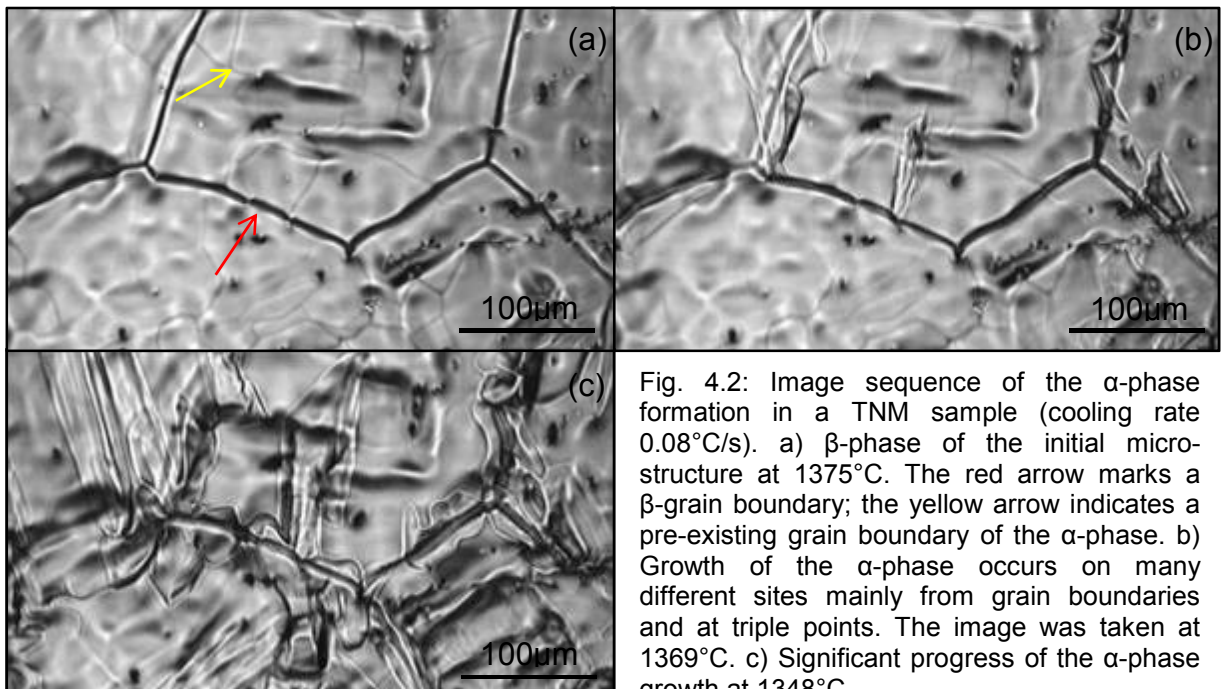

Fig. 4.2: Image sequence of the α-phase formation in a TNM sample (cooling rate 0.08°C/s). a) β-phase of the initial microstructure at 1375°C. The red arrow marks a β-grain boundary; the yellow arrow indicates a pre-existing grain boundary of the α-phase. b) Growth of the α-phase occurs on many different sites mainly from grain boundaries and at triple points. The image was taken at 1369°C. c) Significant progress of the α-phase growth at 1348°C.

boundaries and at triple points. This image was taken at 1369°C, which is 6°C lower or 72s later than when the first nucleation occurred. In Fig. 4.2c) significant progress of the α-phase growth is observed at 1348°C (325s after nucleation occurred). Impingement of different initial α-grains is evident.

4.2.2 Influence of cooling rate

By using 12 different cooling rates between 0.03°C/s and 12.0°C/s, it was possible to create different morphologies within the developing α-phase. This can be attributed to changes in diffusional processes. Ahead of a growing interface a driving force acts to create the equilibrium composition of the growing phase. Diffusion of aluminium in one direction and diffusion of niobium and molybdenum in the opposite direction

control the formation of the developing α-phase and the progression of the phase interface [22,28]. Rejection of refractory metal atoms stabilise the β-phase. The transformation of β- to α-phase occurs by a mechanism controlled by diffusion, even at high cooling rates.

As an example for morphological changes due to a different cooling rates, the development of the α-phase at 0.03°C/s, 1.0°C/s and at 12.0°C/s will be discussed in detail below for the TNM alloy.

Fig. 4.3a) shows a HTLSCM micrograph of the growing α-phase in the TNM alloy at a cooling rate of 0.03°C/s. The video recording of this event can be found on the attached CD as Video A. The image was taken at 1368°C, 11°C below the nucleation temperature. Fig. 4.3b) is a corresponding schematic illustration of the transformation. In this scheme dashed lines represent the former β-grain boundaries, whereas full lines show the evolving α-phase. Since the HTLSCM image is generated
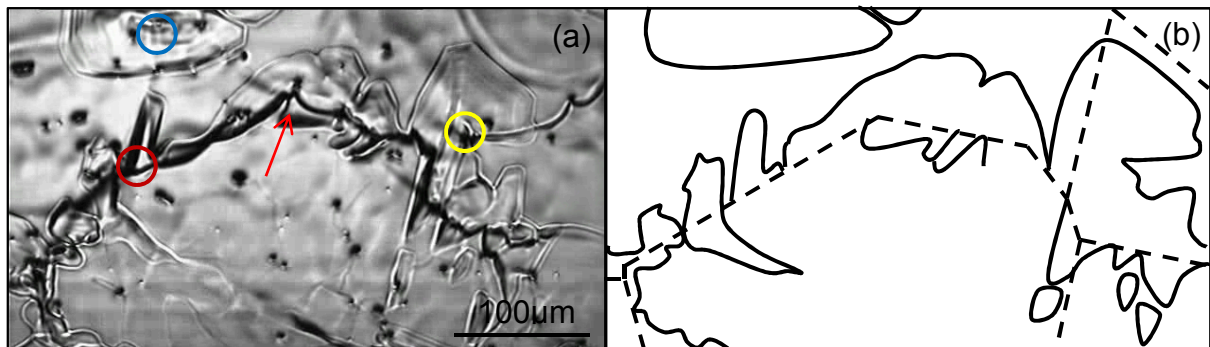

Fig. 4.3: a) HTLSCM micrograph of the evolving α-phase at 1368°C at a cooling rate of 0.03°C/s (TNM alloy). Coloured circles mark different nucleation sites. Blue: nucleation at an inclusion, red: nucleation at a grain boundary, yellow: nucleation at a triple point. The red arrow indicates a pinned grain boundary; b) Schematic representation of the growing α-phase (full lines). Dashed lines correspond to pre-existing grain boundaries within the β-phase.

by the reflection of a laser beam, all kinds of surface roughness is visible. Dark lines are thermal grooves from the pre-existing β-phase grain boundaries. The red arrow in this image marks a spot where the grain boundary is pinned by an obstacle. Transformation fronts between β- and α-phase are evident. The growing α-phase shows no distinct orientation of progression, i.e. growth occurs uniformly until different grains start to impinge upon each other. The phase interfaces are generally planar, which shows that the cooling rate was low enough so that any disturbance of the phase interface is not exaggerated but smoothened. It is evident that nucleation occurs on numerous sites within the previous β-grain. Thus, a grain refining effect is achieved. It shall be noted that phase interfaces that can easily be observed with the eye cannot easily be detected by automated image analysing software. This is because the phases occur in similar grey tones. After the cooling period at 1325°C the amount of α-phase was measured using ImageJ® software. At a cooling rate of 0.03°C/s a phase fraction of 94.0% has transformed to α-phase, the remaining 6% being β-phase. This is a large fraction of the α-phase compared to the phase fraction

diagram in Fig. 2.7a) gained from HEXRD experiments. Different explanations for this effect can be given: Firstly, the phase fraction diagrams were measured during heating, which means that an effect of hysteresis is expected. Secondly, the change in temperature of the HEXRD experiments is higher than the applied cooling rate of 0.03°C/s in the HTLSCM. The phase fraction is thus further in the condition of non-equilibrium.

Fig. 4.4a) shows a HTLSCM micrograph of the growing α-phase in the TNM alloy at a cooling rate of 12.0°C/s. The video recording of this event can be found on the attached CD as Video B. The image was taken at 1327°C, 6°C lower than the temperature at which nucleation took place. Fig. 4.4b) is a corresponding schematic illustration of the transformation. When comparing the morphology of the transformed α-phase resulting from high cooling rates such as 12.0°C/s to those resulting from low cooling rates such as 0.03°C/s, significant differences can be observed. At high cooling rates nucleation is suppressed at high temperatures because of the little time available for the formation of a stable nucleus. At lower temperatures the driving force to create the phase of lowest free energy is higher.

As progression of the phase interfaces occurs faster, less time is available for diffusion (i.e. a shorter diffusion length), thus finer structures are favoured. Phase interfaces show a distinct direction of progression, which leads to a lath-like morphology
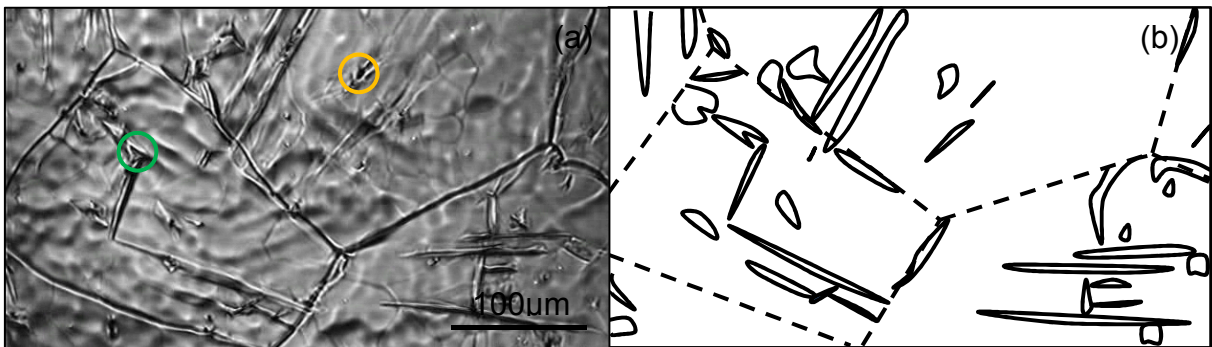

Fig. 4.4: a) HTLSCM micrograph of the evolving α-phase at 1327°C at a cooling rate of 12.0°C/s (TNM alloy). Phase interfaces are sharp, showing a distinct direction of progression. The green circle marks a point were nucleation must have occurred underneath the surface. The orange circle marks a lath that grows perpendicular to the surface and impinges. b) Schematic representation of the growing α-phase (full lines). Dashed lines correspond to former grain boundaries within the β-phase.

similar to a basket-weave structure, well-known in titanium alloys [12]. These structures are often referred to as Widmanstätten α-laths. Furthermore laths that progress perpendicular to the surface impinge with the surface as marked with the orange circle in Fig. 4.4a). In Fig. 4.4 it is visible that there is a specific angular relationship between the laths. This observation can be attributed to the nature of Widmanstätten laths, which prefer crystallographic directions that allow them to grow fastest. The fact that these laths grow in distinct directions is in practice not especially favourable because that leads to many α_2/γ-colonies of the same orientation. This phenomenon reduces the grain refining effect that can be achieved by the $\beta \rightarrow \alpha$ phase

transformation [9]. In general it can be stated that the growth of Widmanstätten laths is governed by the kinetics of discontinuous precipitation reactions, whereas equiaxed structures, which are observed at lower cooling rates, progress according to the laws of spherical growth. Both types of growth can either be controlled by the kinetics of diffusional transport or by interface mobility [9].

Following the cooling step, the amount of α-phase was reduced to 19.1%, which is significantly lower than that observed at lower cooling rates and lower than the phase fraction shown in Fig. 2.7a). This indicates that a cooling rate of 12.0°C/s is high enough to supress the transformation of a significant amount of β-phase. The β-phase is thermodynamically unstable, but kinetics hinders its transformation.

At intermediate cooling rates between 0.67°C/s and 1.67°C/s both morphological features, planar and lath-like structures, are found. Fig. 4.5a) shows a HTLSCM micrograph of such a structure, recorded at a cooling rate of 1.0°C/s and Fig. 4.5b) shows a corresponding schematic illustration. The video recording of this event can be found on the attached CD as Video C. The image was taken at 1344°C, 18°C lower than the onset temperature of transformation. Frequently, lath-like structures as well as planar structures nucleated at a grain boundary beneath the surface. This observation is adressed in more detail in subchapter 4.2.3. Widmanstätten laths started to grow earlier than the planar growth fronts during cooling. The amount of
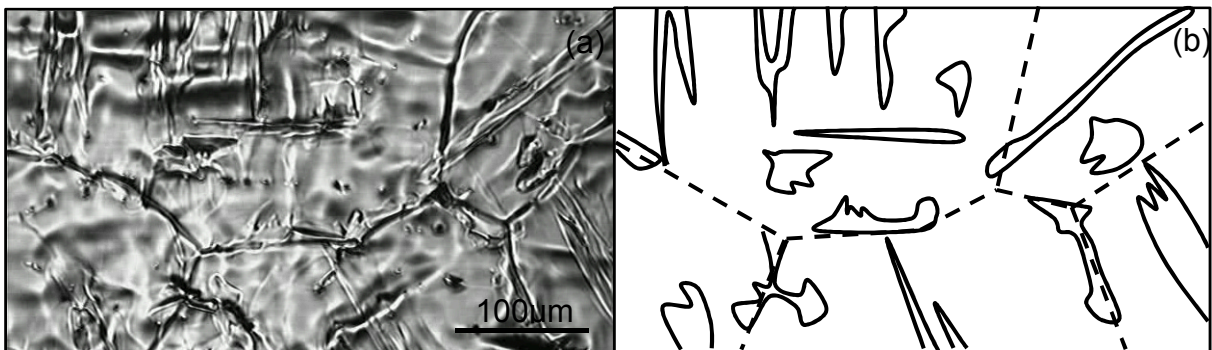

Fig. 4.5: a) HTLSCM micrograph of the developing α-phase at 1344°C at a cooling rate of 1.0°C/s (TNM alloy). Both morphological features (lath-like and planar) are observed. b) Schematic representation of the growing α-phase in full lines. Dashed lines correspond to former grain boundaries within the β-phase.

α-phase is found to be an intermediate value of 79.1% lying between very high cooling rates and close to equilibrium cooling rates. This phase fraction is close to the phase fraction displayed in the phase fraction diagram in Fig. 2.7a).

Neither of the β-solidifying alloys (TNM and TN1.5Mo0.5C) show significantly differ-ent morphologies which could be attributed to their composition. Both alloys show the same trend towards lath-like structures at high cooling rates. Since the equilibrium transformation temperature differs by about 52°C, as estimated from the lowest cooling rate, diffusion coefficients would differ even if the composition was the same. Thus, no quantitatively comparable information about structure spacing or interface

progression can be gained. Videos with the equivalent cooling rates for the TN1.5Mo0.5C alloy can be found on the attached CD as Videos D, E, and F.

4.2.3   Preferred nucleation sites and the role of boron addition

At low cooling rates nucleation to typically takes place on precipitates, grain boundaries and triple points. Alloying with boron leads to dispersions of mainly titanium boride (TiB) and titanium diboride (TiB$_2$) types in TiAl alloys. The composition of the borides that were observed in the TNM alloy was confirmed by EDX analysis. Only borides of TiB type were observed. Additionally precipitation of carbides was found to occur in carbon containing alloys. The occurrence of high temperature carbides will be discussed in subchapter 4.2.4. Nucleation from precipitates and dispersions was found to qualitatively require the lowest undercooling. As a result, growth from these nucleation sites occurs first. A low undercooling corresponds to a low overall free energy needed to create a critical nucleus. At higher cooling rates the same mechanisms are still operating, but a significantly larger number of grains were found to nucleate beneath the surface. This is thought to be an effect of sample thickness. Along the thickness of the sample a thermal gradient is generated so that a higher undercooling is achieved underneath the surface. Once the grains impinge with the free surface they can be detected in the HTLSCM. In Fig. 4.3a) and Fig. 4.4a) this effect is visualized with coloured circles. Blue, red and yellow circles mark spots where nucleation was observed to occur first on the surface. Green and orange circles indicate spots where it is very likely that nucleation first occurred underneath the surface. This can readily be seen by looking at the image sequences. At intermediate cooling rates, the morphology of the growing α-phase is dependent on whether nucleation occurs on grain boundaries or underneath the surface (Fig. 4.5). While both morphological features are found to occur, Widmanstätten laths are more frequently observed to nucleate from beneath the surface, whereas planar structures more often nucleate at grain boundaries and triple points on the surface.

4.2.4   Formation of hexagonal carbides

Carbon is often alloyed to TiAl alloys to improve creep resistance and strength at elevated temperatures. This allows enlargement of the window of usage for this alloy group. Carbon is found either as an interstitial element in solution homogeneously distributed, or as carbide, depending on the solubility of the constituent phases at a given temperature [6]. At high temperatures so called hexagonal (H) carbides of Ti$_2$AlC structure can form.

Within the experimental series on phase transformations precipitation of a second phase occurred when heating a sample of the initial cast and HIPed microstructure as shown in Fig. 4.1c). According to the phase fraction diagram of the TN1.5Mo0.5C

alloy as shown in Fig. 2.7c) at 1475°C only β-phase is present. One sample of TN1.5Mo0.5C was annealed at 1475°C for 1h in the infrared furnace of the HTLSCM and a large amount of precipitates was found to form. These precipitates are dark in appearance, which can be attributed to a low reflectivity in the range of the wavelength of the laser. In Fig. 4.6 a HTLSCM micrograph of the precipitates under consideration is shown. These elongated, presumably plate-like precipitates strongly interact with the remaining grain boundaries by pinning. This pinning is so strong that virtually no grain boundary movement could be observed any more, even though the shape of the boundaries indicates that they are not in thermodynamic equilibrium. Following the heat treatment, the samples were prepared as described in subchapter 3.3.1 for the FEG-SEM. EDX maps were taken of precipitates revealing their chemistry as being the one associated with H carbides (within the accuracy of the EDX). Chemical compositions as measured with EDX are given in Table 4.1. Additionally, niobium is present in the observed precipitates, whereas no molybdenum is detected.
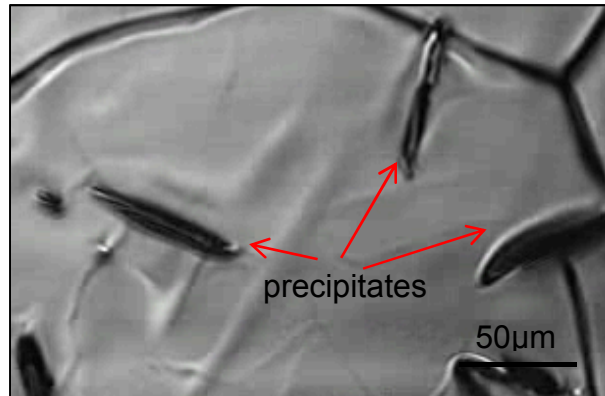

Fig. 4.6: Precipitates as observed after annealing the TN1.5Mo0.5C alloy at 1475°C for 1h.

SEM micrographs of the microstructure after annealing are shown in Fig. 4.7. Rod-shaped precipitates of up to 100µm in length and 10µm in width have been observed and they are uniformly distributed. The bright phase in Fig. 4.7 is the β_0-phase, grey equiaxed structures are α_2/γ-colonies and dark elongated precipitates are H carbides. After an annealing of 1h at 1475°C and subsequent cooling with a rate of 1.67°C/s to room temperature, coarse carbides show distinct habit planes in accordance to their hexagonal lattice structure. Carbides precipitate from the β-matrix, since the solubility of carbon in the β-phase is very low and hence, the decomposition into two phases is energetically favourable. Compared to the initial microstructure shown in Fig. 4.1c), significant grain coarsening has occurred. The microstructure has the same appearance as a cast structure.

In Fig. 4.7b) borides are marked with red circles. These particles were also identified using EDX analysis as being of TiB structure. It appeared as if borides might act as nucleation sites for the observed carbides.

Table 4.1: Composition of precipitates as measured by EDX scan.

titanium [at%]	aluminium [at%]	carbon [at%]	niobium [at%]
49.58	24.58	23.77	2.06

One additional feature that has been observed and is shown in Fig. 4.7b) is that all γ-lamellae (orientation indicated by red dashed lines) within one grain are oriented parallel to the long axis of the previously precipitated carbides. This effect can be explained by the following mechanism: At 1475°C only β-phase is present. Grain coarsening occurs until hardly any grain boundaries are present. Remaining grains do not coarsen any further, as the boundaries are pinned by precipitated carbides. Due to the different orientations of the carbides it is assumed that the image section shown in Fig. 4.7a) corresponds to several previous β-grains. The carbides grow into the matrix, showing the same orientation relationship (OR) with the β-phase, which is generally associated with α growth (Burgers orientation relationship), which is given in Eq. 2.2 [29]. Due to the hexagonal crystal lattice of the carbides it appears to be plausible that specific growth orientations are energetically favourable as it is the case when the α-phase grows into the β-matrix. However, it has to be mentioned that the orientation of the carbides might not be controlled solely by the similarity of crystal lattices. The morphology of a second phase particle is also influenced by the
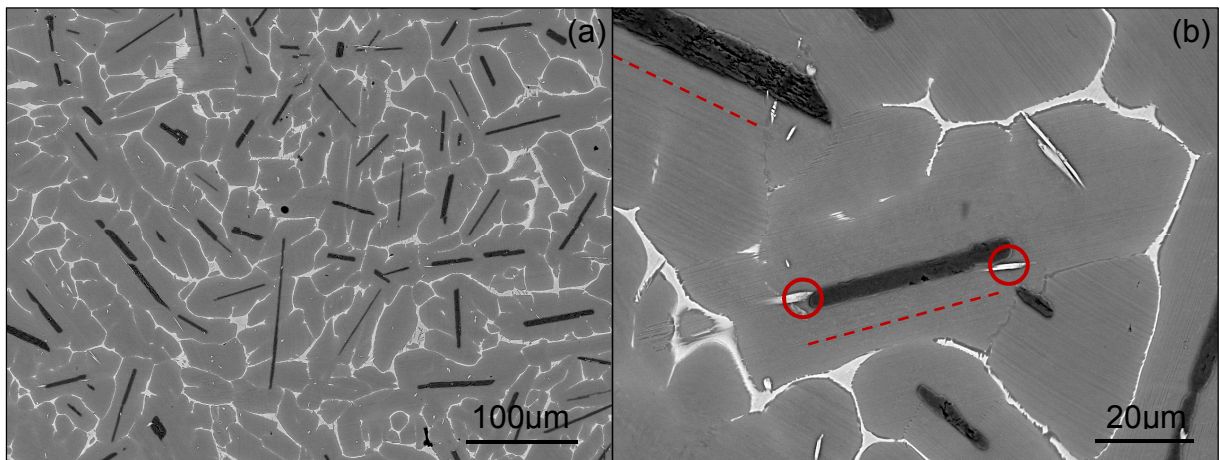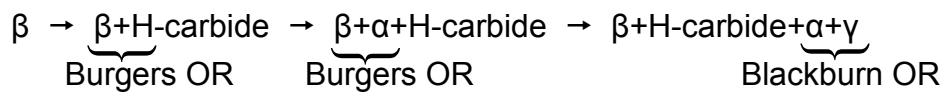

Fig. 4.7: FEG-SEM micrographs of a TN1.5Mo0.5C sample after heat treatment at 1475°C for 1 hour and cooling to room temperature with a rate of 1.67°C/s. The bright phase is the β_0-phase; grey grains are α_2/γ-colonies. Elongated dark precipitates are H carbides. b) Borides, which may act as nucleation sites are marked by red circles; in b) parallel arrangement of γ-lamellae and H carbides is visible. The orientation of the γ-lamellae is indicated by red dashed lines. The images were taken in BSE mode.

nature and density of bonds across a certain interface, which corresponds to the interfacial energy. Observations in the HTLSCM have shown that during cooling, the α-phase nucleates almost exclusively on H carbides through heterogeneous nucleation, indicating that a specific orientation relationship is preferred. It is evident that nucleation at the surface of a H carbide requires the lowest energy for nucleation. Following the formation of the α-phase, some α-phase transforms into the

γ-phase by the diffusional growth of γ-lamellae. This formation follows the well-known Blackburn orientation relationship, as given in Eq. 2.3. Hence, the reason for the obtained parallel carbide/γ-lamellae structure is the hexagonal lattice of the H carbides and their orientation relationship with the β parental phase of body centred cubic lattice. A complex hierarchical sequence of orientation relationships of the involved phases follows. This effect is generally not observed in the case of nucleation of the α-phase on the surface of borides [9]. The previously described sequence of transformations with the occurring orientation relationships denoted beneath can be summarised as given in the following sequence: Transformation of β- and α-phase to their ordered counterparts is not taken into account, since these transformations are not visible using optical microscopy.

$$\beta \;\rightarrow\; \underbrace{\beta+\text{H-carbide}}_{\text{Burgers OR}} \;\rightarrow\; \underbrace{\beta+\alpha+\text{H-carbide}}_{\text{Burgers OR}} \;\rightarrow\; \beta+\text{H-carbide}+\underbrace{\alpha+\gamma}_{\text{Blackburn OR}}$$

The resulting orientation relationship between H carbide and γ-phase has previously been reported and is described in detail in references [41,42]. In terms of crystallography the resulting orientation relationship between H carbide and γ-phase can be noted as given in Eq. 2.5.

4.2.5 Evaluation of continuous cooling transformation diagrams

Continuous cooling transformation (CCT) diagrams are of great value for the optimal design of a range of processing steps such as forging, casting and subsequent heat treatments. Continuous cooling transformation generally is of greater industrial importance than isothermal transformation, because many processes such as heat treatments or cooling after welding utilize continuous cooling ramps. However, equations that describe nucleation and growth during continuous cooling are difficult to derive, since parameters such as the driving force, undercooling and diffusion coefficients continuously change during the cooling cycle. Hence, CCT diagrams have to be measured experimentally or simulated for each material under the conditions of interest. Typically CCT diagrams are derived by the use of dilatometry or DSC experiments. However, HTLSCM experiments provide similar data, with the advantage that the transformation processes can be followed *in-situ* in the microscope. Consequently, this approach has been followed in order to obtain CCT diagrams for the onset of the β → α phase transformation of the TNM and the TN1.5Mo0.5C alloy.

Samples were cooled from the β-phase field region into the α+β phase field region, as described in subchapter 3.2.3.1. Subsequently the sequences of images were analysed in order to find the onset temperature of the phase transformation. From the

captured cooling profile data the corresponding time to the onset of transformation was calculated. Accuracy of the determined temperatures is in the range of ±5°C.

One limitation of the system is that the cooling rates are not linear at cooling rates higher than 1.67°C/s, because the controlling unit cannot control the power input of the halogen lamp at such high cooling rates (see also subchapter 3.2.5). However, the experiments carried out showed that the first 40°C of the cooling sequence show an approximately linear gradient.

The CCT diagram of the TNM alloy is shown in Fig. 4.8a). The solution temperature (T_1) was chosen to be 1405°C for a solution time (t_1) of 300s. Blue crosses correspond to the onset of phase transformation for a given cooling rate which is labelled in the diagram at each corresponding line. For the highest three cooling rates (non-linear behaviour) the cooling rate was determined using Eq. 4.1, where T' is the cooling rate, T_1 is the annealing temperature, T_{onset} is the temperature at the onset of transformation and Δt is the cooling time between start of the cooling sequence and the onset of transformation.

$$T' = \frac{T_1 - T_{onset}}{\Delta t} \hspace{5cm} (4.1)$$

The line representing the cooling sequence in the diagram, however, is the real captured cooling profile, which is thus not linear.

The transformation temperature at the lowest cooling rate (0.03°C/s) is found to be in good agreement with equilibrium transformation temperatures reported in reference [8]. With increasing cooling rate a significantly higher undercooling is necessary for the formation of the α-phase. The highest undercooling was 46°C with respect to the transformation temperature observed for near equilibrium conditions (at a cooling
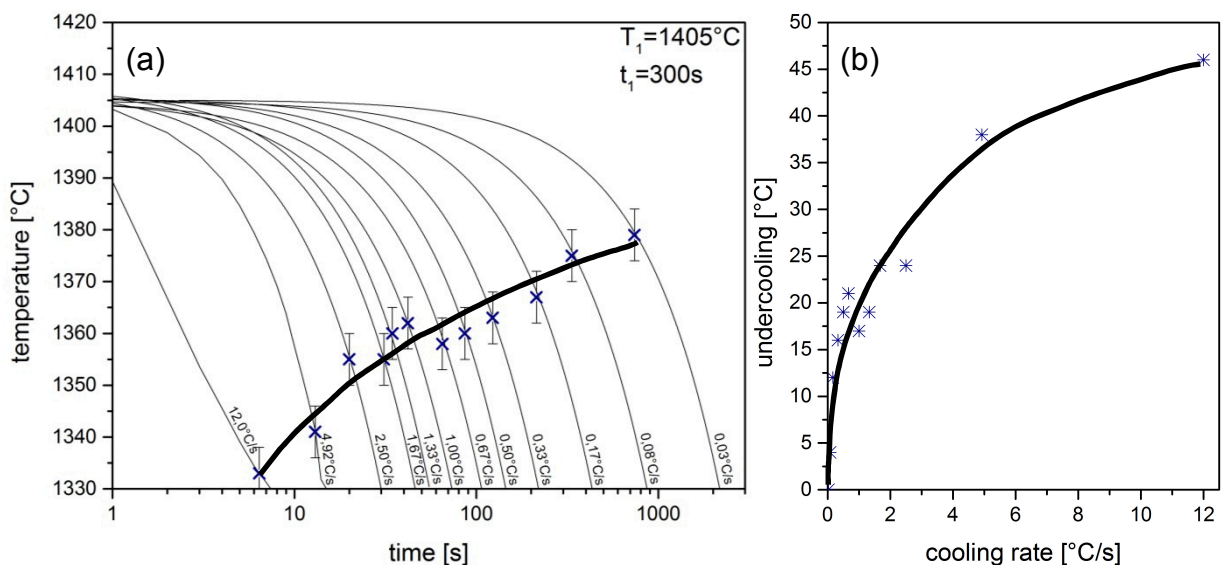

Fig. 4.8: a) CCT diagram of the TNM alloy. Blue crosses represent the onset of α-phase formation. The solution temperature T_1 was 1405°C; the solution time t_1 was 300s. Cooling rate values are given on the lower end of each corresponding line. b) dependence of undercooling on the cooling rate.

rate of 0.03°C/s) and this undercooling is shown as a function of the cooling rate in Fig. 4.8b). The undercooling required for the onset of phase transformation is a direct consequence of the time dependent step for nucleation. At a certain temperature during the cooling sequence the driving force for transformation is always the same. However, the formation of a critical size of nucleus involves the motion of single atoms, which is a time dependent step and hence, the size of a critical nucleus is strongly influenced by the applied undercooling. These effects govern the process of nucleation [22,27].

The CCT diagram of the TN1.5Mo0.5C alloy is shown in Fig. 4.9a). The solution temperature (T_1) was 1475°C and the solution time (t_1) was 60s. The significantly shorter solution time was necessary in order to create a comparable β-phase microstructure, since grain growth occurs at higher rates under these conditions (see also subchapter 4.5). The lowest cooling rate (0.03°C/s) is close to equilibrium conditions. The highest undercooling of 31°C, was obtained at a cooling rate of 11.54°C/s. The undercooling is shown as a function of the cooling rate in Fig. 4.9b). For this
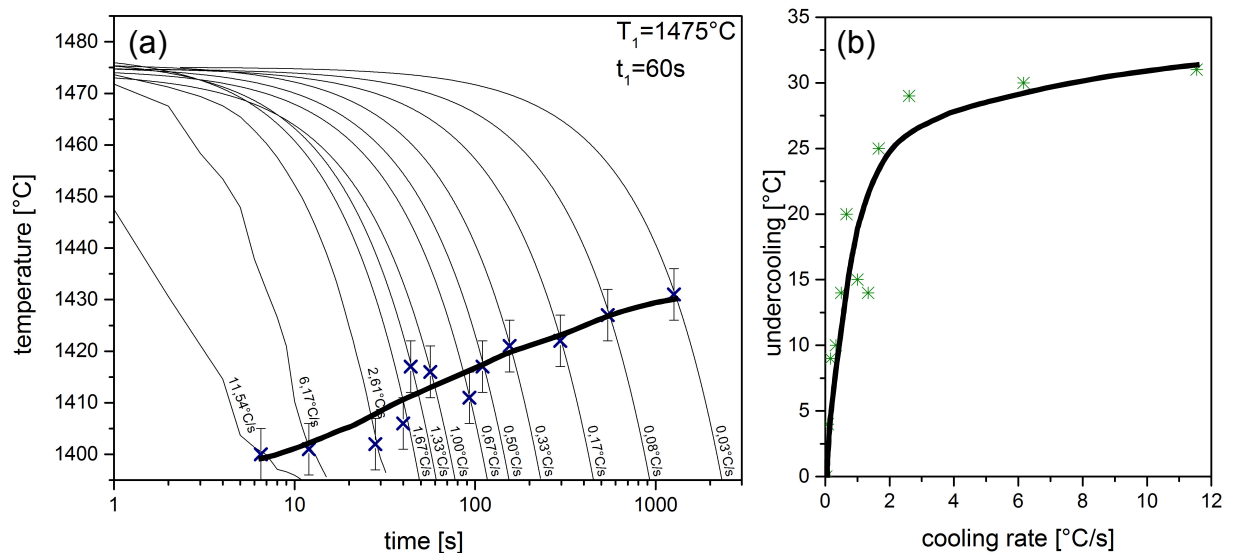

Fig. 4.9: a) CCT diagram of the TN1.5Mo0.5C alloy. Blue crosses represent the onset of α-phase formation. The solution temperature T_1 was 1475°C; the solution time t_1 was 60s. Cooling rate values are given on the lower end of each corresponding line. b) dependence of undercooling on cooling rate.

evaluation of the undercooling the transformation temperature at a cooling rate of 0.03°C/s is taken as a reference temperature.

The experimentally determined transformation temperatures as a function of the cooling rate for alloys TNM and TN1.5Mo0.5C are summarized in Table 4.2.

Table 4.2: Temperatures for the onset of α-phase formation. $T_β$ is the nucleation temperature of the α-phase. The label $T_β$ refers to its meaning as β-transus temperature.

cooling rate [°C/s]	$T_β$ (TNM) [°C]	$T_β$ (TN1.5Mo0.5C) [°C]
0.03	1379	1431
0.08	1375	1427

Continuation of Table 4.2.

cooling rate [°C/s]	T_β (TNM) [°C]	T_β (TN1.5Mo0.5C) [°C]
0.17	1367	1422
0.33	1363	1421
0.50	1360	1417
0.67	1358	1411
1.00	1362	1416
1.33	1360	1417
1.67	1355	1406
2.50/2.61*	1355	1402
4.92/6.17*	1341	1401
12.00/11.54*	1333	1400

* first cooling rate applies to the TNM alloy, second cooling rate applies to the TN1.5Mo0.5C alloy

4.3 γ-phase formation

The γ-phase is the major phase at room temperature in TNM alloys and derivatives. In the TNM alloy this intermetallic phase becomes thermodynamically stable at about 1255°C and at slightly higher temperatures for the TNM0.5C and the TN1.5Mo0.5C alloys as shown in the phase fraction diagrams in Fig. 2.7. Cooling experiments for all three alloys were carried out in the HTLSCM in order to elucidate the growth of the γ-phase *in-situ*. Experiments were performed at cooling rates of 12.5°C/s and 0.17°C/s. In the following subchapter the focus will be on describing morphological differences and relating them to the differences in composition of the alloys.

4.3.1 Qualitative description of the γ-phase formation

The temperature of the onset of γ-phase formation was determined from cooling a sample of the TNM alloy at a rate of 0.17°C/s from 1300°C to a final temperature of 1150°C. The first visible γ-lamellae occurred at about 1190°C. This observation is neither in agreement with the transformation temperature in the phase fraction diagram shown in Fig. 2.7a) nor with transformation temperatures in [49], where transformation temperatures of a TNM alloy were determined using neutron-diffraction. The reason is the surface sensitivity of observations in the HTLSCM. At the temperature under consideration thermal etching is a slow process, and hence, features become visible only delayed. However, the experiment showed that the chosen temperature regime is suitable for the observation of the γ-phase formation.

Growth of the γ-phase in the TNM alloy after rapid cooling (12.5°C/s) from 1300°C to 1150°C was investigated. At 1300°C the microstructure consists mainly of α-phase with a small amount of β-phase aligned along the α grain boundaries. The presence of this two phase field region follows from the phase fraction analysis shown in Fig. 2.7a). At 1150°C the γ-phase is thermodynamically stable. Two images of the transformation process are shown in Fig. 4.10. The frame shown in Fig. 4.10a) was taken 80s and the one in Fig. 4.10 b) 125s after cooling started. The full sequence of

events is shown in Video G on the CD that is attached to this thesis. γ-lamellae nucleate mainly on grain boundaries as indicated in Fig. 4.10a) with a yellow circle. Nucleation can also occur on second-phase particles, as indicated by the green circle. All γ-lamellae that formed in a previous α-grain are aligned parallel, displaying the Blackburn orientation relationship [32]. Interlamellar spacing can only be seen in some grains because the images were taken at a magnification of 340, which is too low to resolve all the interlamellar spacings. However, the observed growing γ-structures are more likely to be colonies of parallel growing γ-laths than individual
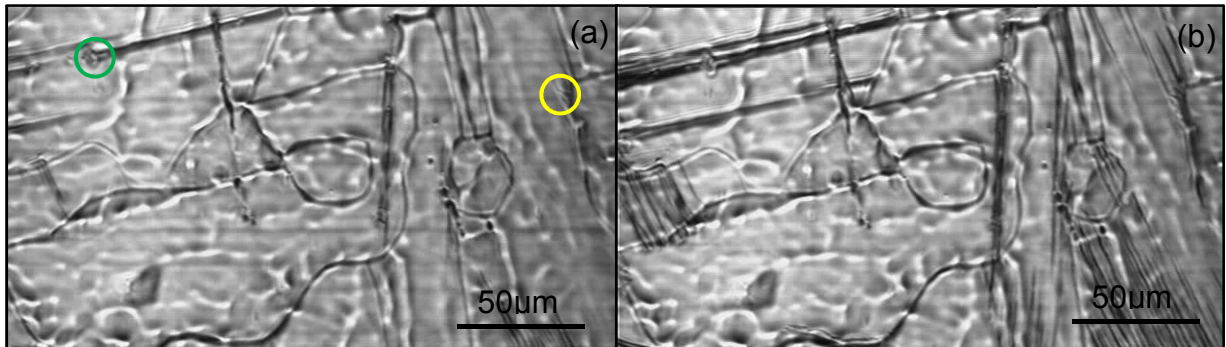

Fig. 4.10: Growth of the γ-phase in the TNM alloy at a) 80s and b) 125s after rapid cooling from 1300°C to 1150°C. In a) yellow circle marks nucleation from grain boundary; green circle marks nucleation from second phase particle.

laths. Significant differences in microstructural development have been observed when the TN1.5Mo0.5C alloy was subjected to the same heat treatment as the TNM alloy. An image sequence showing growth of the γ-phase is displayed in Fig. 4.11. The full sequence of events is shown in Video H on the CD that is attached to this thesis. Fig. 4.11a) was taken 275s and Fig. 4.11b) 508s after a rapid drop in temperature below the α-transus temperature (from 1300°C to 1150°C). The actual applied cooling rate was 12.5°C/s. However, the actual cooling rate is of minor importance as the growth only occurs in the range of minutes after the cooling period. At a temperature of 1150°C the γ-phase is thermodynamically stable. Growth apparently initiates later than in the TNM alloy, which has to be related to changes in diffusional processes induced by alloying with carbon and an increased amount of molybdenum. A globular morphological phase is indicated by blue circles in Fig. 4.11a), which is visible significantly earlier than lamellar γ-structures. These grains show a nearly equiaxed structure, which entirely grew at grain boundaries soon after cooling. Subsequent SEM images identified these globular structures as γ-grains. Only after about 8min lamellar γ-colonies grow into the α-matrix. However, it can be assumed that very fine γ-lamellae can start growing at an earlier stage. Indicated with red arrows in Fig. 4.11b) are lamellar colonies that are coarse enough to be resolved with the HTLSCM. In the TN1.5Mo0.5C alloy the interlamellar spacing in colonies is lower than the resolution of the microscope at a magnification of 340. The decreasing interlamellar spacing in comparison with carbon free alloys, was attributed to the role

of the alloying element carbon by a mechanism, that increases the likelihood of nucleation events through the formation of stacking faults [50]. The delayed growth of the γ-phase as well as the decreasing interlamellar spacing within the γ-phase, with
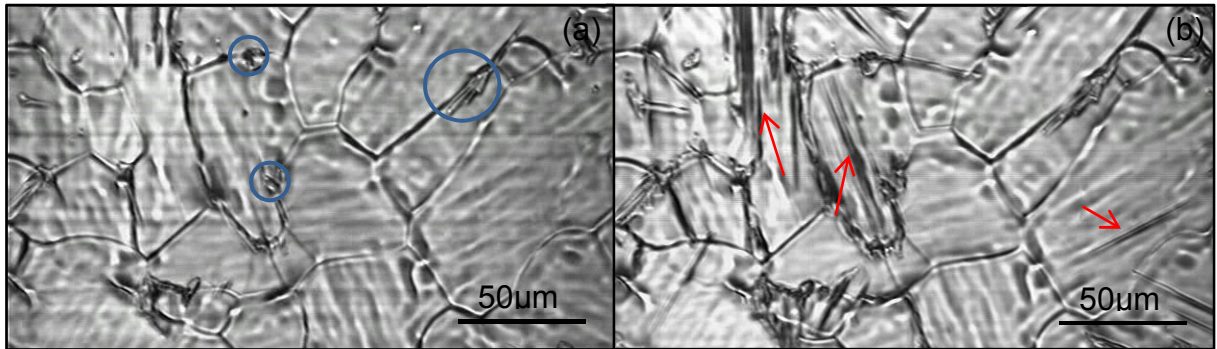

Fig. 4.11: Growth of the γ-phase in the TN1.5Mo0.5C alloy at a) 275s and b) 508s after rapid cooling from 1300°C to 1150°C. In a) blue circles indicate the occurrence of a different morphology; in b) red arrows indicate lamellar growth.

reference to the TNM alloy, are assumed to be a result of changes in diffusion rates.

A similar experiment was carried out on the TNM0.5C alloy. A significantly different microstructure was obtained, since annealing at 1300°C occurred in single α-phase field region rather than in a two phase field region as it was the case for the other alloys. A sequence of images showing the formation of the γ-phase is shown in Fig. 4.12, but the full sequence of events is shown in Video I on the CD that is attached to this thesis. Fig. 4.12a) was taken 130s and Fig. 4.12b) 560s after a rapid drop in temperature below the α-transus temperature. The cooling rate was evaluated to be 12.5°C/s. As the growth of the γ-phase occurred only after minutes at 1150°C the actual cooling rate is of little importance. The occurrence of a single α phase field region can readily be seen in the phase fraction diagram in Fig. 2.7b). Grain growth occurs much faster in this regime. This topic is the subject of subchapter 4.5.1. Hence, a smaller amount of nucleation sites for the γ-phase is available. The growth morphology is generally similar to that observed in the TNM alloy, growth in the TNM0.5C however, is faster than in the TN1.5Mo0.5C alloy. It is assumed that slower transformation is a consequence of a reduced rate of diffusion in the TN1.5Mo0.5C alloy and thus the slower growth cannot be attributed to the carbon addition.
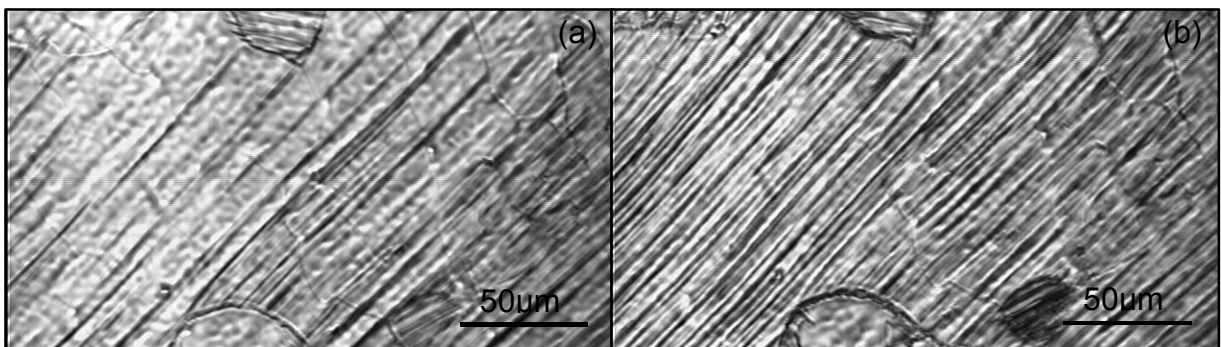

Fig. 4.12: Growth of the γ-phase in the TNM0.5C alloy at a) 130s and b) 560s after rapid cooling from 1300°C to 1150°C.

The effect of a lower cooling rate is readily visible. Qualitatively the interlamellar spacing increases with decreasing cooling rate, which can be easily explained by a longer diffusion length. However, due to the limited resolution of the HTLSCM no quantitative information could be obtained and is therefore not discussed in detail.

4.3.2 γ-formation and cellular reaction after quenching and annealing

Quenching and annealing was carried out on TNM samples in order to investigate the occurrence of the cellular reaction. This reaction is of industrial relevance, because it was reported to increase the room temperature ductility without a negative effect on tensile strength and creep resistance [39].

At sufficiently high cooling rates the formation of a lamellar structure as well as a massive γ-phase morphology is supressed. A large amount of supersaturated α-phase is then present at room temperature. However, this structure is thermodynamically instable and will transform into γ-phase if sufficient thermal activation is provided. The effective suppression of the γ-formation by utilization of the heat treatment described in subchapter 3.4 was proven by FEG-SEM and is shown in Fig. 4.13a). Samples of the TNM alloy were annealed at 1290°C for a duration of 10min. Thereafter they were quenched in water. The dark grey grains in Fig. 4.13a) are supersaturated α-phase, whereas the bright phase is the retained β-phase. Within the α-phase there are no substructures visible that can be attributed to γ-phase in comparison with the initial microstructure in Fig. 4.1a). These supersaturated samples were afterwards subject to an annealing procedure as described in detail in the following paragraph.

Supersaturated samples were annealed at different temperatures, which leads to the precipitation of very fine γ-lamellae. Fig. 4.13b) shows a SEM micrograph of a TNM sample that was annealed for 15min at 950°C and thereafter cooled at a rate of 1.67°C/s. The fine γ-lamellae are below the resolution limit of the SEM used, thus they cannot be visualized. At the same time as the precipitation of γ-phase takes place a cellular reaction occurs. In TNM alloys this reaction is a discontinuous coarsening process. The fine lamellar colonies are transformed starting from the colony boundaries by the motion of a reaction front [39]. The initial cellular reaction can be identified in Fig. 4.13b).

Annealing of quenched samples was also carried out at 1150°C. These samples were cooled afterwards with a cooling rate of 1.67°C/s. The annealing process retransforms the microstructure to a similar one as the initial microstructure as expected, since the initial HIP process takes place at 1200°C. This is shown in Fig. 4.13c). The microstructure exhibits α_2/γ-colonies and a significant amount of β-phase with embedded equiaxed γ-grains. Remaining features of the cellular reaction are aligned at the colony boundaries. At this temperature the thermal activation for

diffusional processes to occur is very high. Hence, all thermally activated processes are shifted to significantly shorter times. Additionally, it can be observed that the γ-lamellae after annealing at 1150°C are significantly coarser than after annealing at 950°C. This is due to the fact that at elevated temperatures the diffusion length is significantly larger.
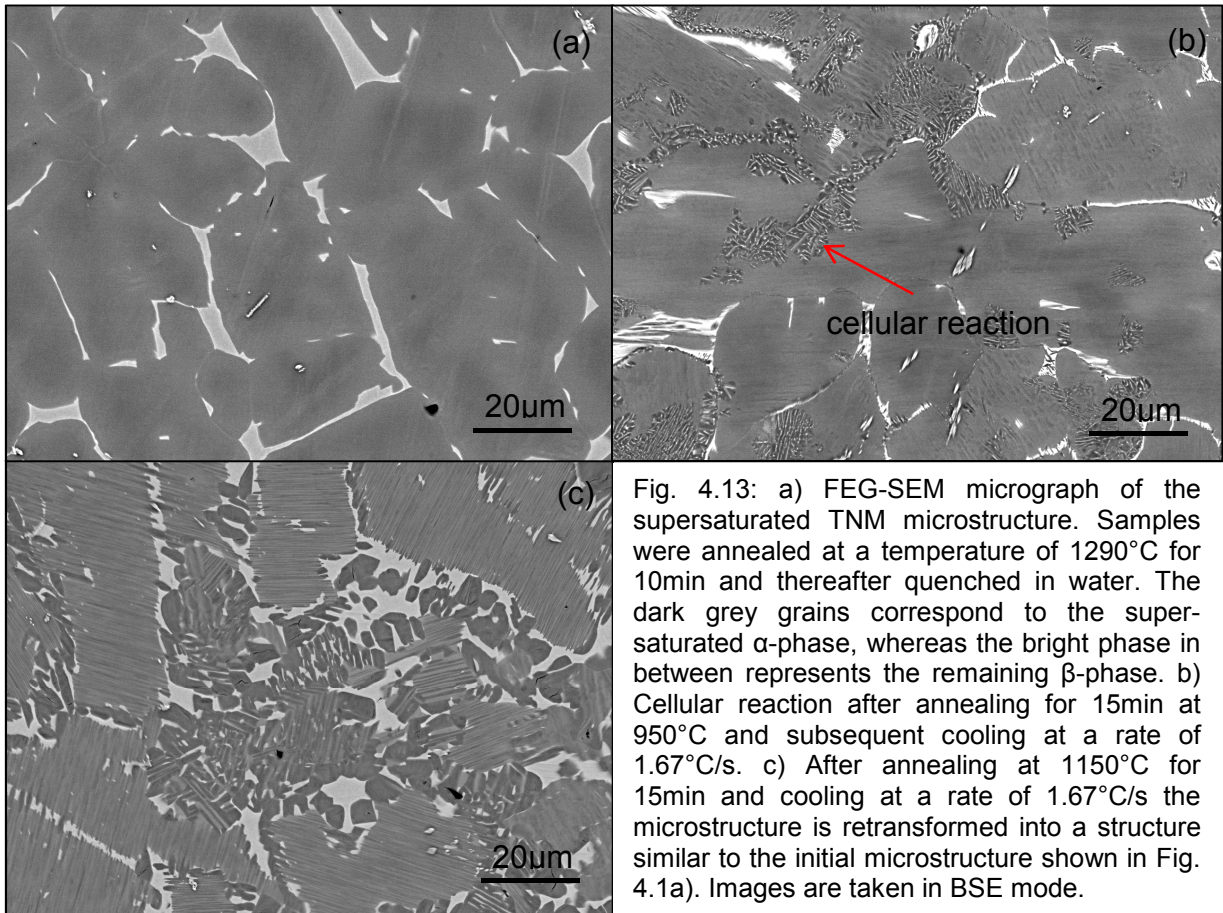
Fig. 4.13: a) FEG-SEM micrograph of the supersaturated TNM microstructure. Samples were annealed at a temperature of 1290°C for 10min and thereafter quenched in water. The dark grey grains correspond to the super-saturated α-phase, whereas the bright phase in between represents the remaining β-phase. b) Cellular reaction after annealing for 15min at 950°C and subsequent cooling at a rate of 1.67°C/s. c) After annealing at 1150°C for 15min and cooling at a rate of 1.67°C/s the microstructure is retransformed into a structure similar to the initial microstructure shown in Fig. 4.1a). Images are taken in BSE mode.

Part II: Grain boundary motion and grain growth

From a processing point of view grain growth is a crucial topic, since all materials undergo processing steps at elevated temperatures at some stage during their production and/or subsequent heat treatments. TiAl alloys are especially prone to losing ductility if large and inhomogeneous microstructural features are present. Coarse structures can lead to the initiation of cracks and must therefore be avoided [35]. At high temperatures grain growth occurs at high rates due to thermally activated grain boundary motion. Hence, understanding grain coarsening is essential for the prediction of the microstructural evolution.

4.4   Grain boundary motion at 1300°C

Isothermal annealing of TNM, TNM0.5C and TN1.5Mo0.5C samples was performed at 1300°C at a heating rate of 1.67°C/s. This temperature regime is of special interest for both forging and heat treatment of TNM alloys. Forging at this temperature is favourable if β-phase is present. Because of its bcc crystal lattice this phase provides enough independent slip systems for deformation. At this temperature the TNM and the TN1.5Mo0.5C alloy exhibit an α+β phase field region. The β-phase shows a sluggish dissolution behaviour due to the stabilization with niobium and molybdenum, which diffuse slowly. In addition no α single phase field region occurs as shown in Fig. 2.7a) and c). In contrast the TNM0.5C alloy shows an α single phase field region (see Fig. 2.7b)). The occurrence of small amounts of β-phase during forging and heat treatments was shown to effectively supress grain growth in the α-phase due to alignment of the β-phase alongside the grain boundaries of the α-grains [14,16]. For the quantification of grain growth the chosen approach in this thesis project was to study grain boundary motion. Grain boundary motion is equivalent and represents growth and shrinkage of grains [25]. This approach is designed to determine the time dependence of grain growth, but does not directly reflect the grain size or size distribution at a certain time. The reason for choosing this approach is that the effect of thermal etching is small in the TNM0.5C alloy at the temperature under consideration. This is because the grain boundaries are very mobile and thermal grooving is time dependent. Hence, high magnifications of 340 have been used, which means that only very few grains are observed. Grain boundary motion is tracked by following the motion of triple points in order to be able to follow exactly the same point of the grain boundary at all times. It is therefore assumed that the grain boundary junction does not affect the mobility of the grain boundary [25]. This assumption seems to be reasonable, because the observed angles at a triple point always remain close to 120°. In Fig. 4.14 HTLSCM images of all three alloys at 1300°C are shown; Fig. 4.14a) the TNM alloy, Fig. 4.14b) the TN1.5Mo0.5C alloy and Fig. 4.14c) TNM0.5C

alloy. Red arrows in Fig. 4.14a) and Fig. 4.14b) indicate β-phase aligned along the grain boundary. The blue arrow marks a triple point as observed in the TNM0.5C alloy. By using a MATLAB® script the displacement of grain boundary junctions is tracked on single frames extracted from HTLSCM videos. This displacement is plotted as a function of time in Fig. 4.15a) for the TNM0.5C alloy. Two grain boundary
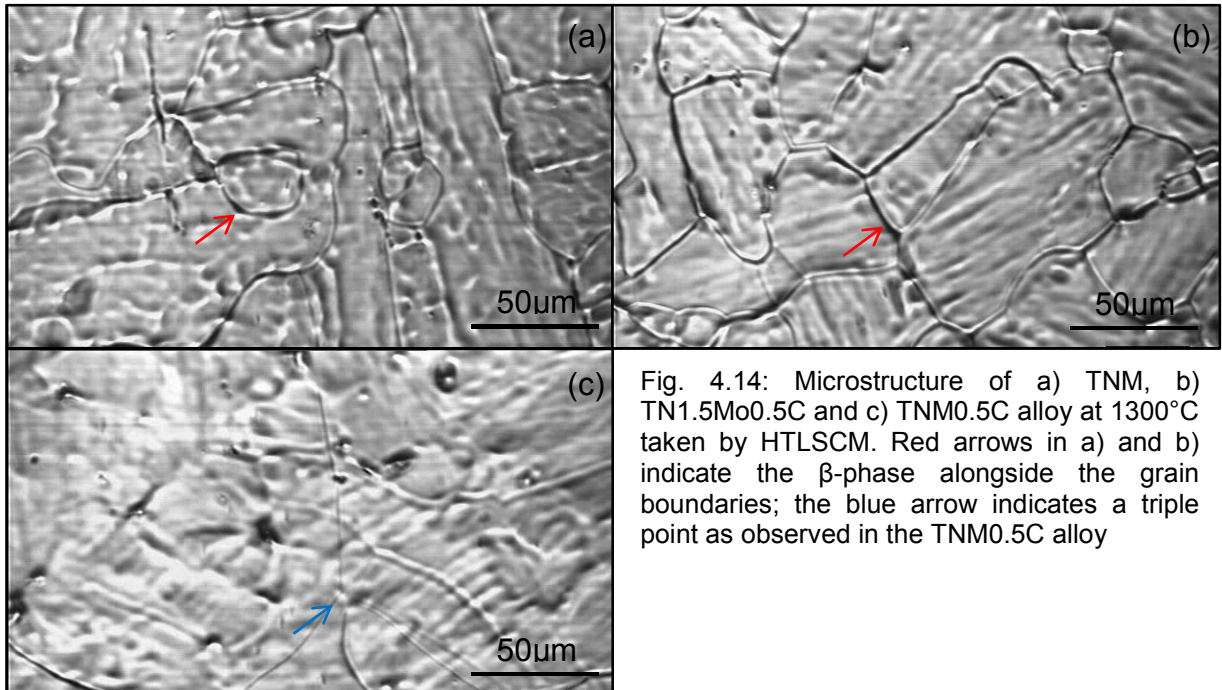

Fig. 4.14: Microstructure of a) TNM, b) TN1.5Mo0.5C and c) TNM0.5C alloy at 1300°C taken by HTLSCM. Red arrows in a) and b) indicate the β-phase alongside the grain boundaries; the blue arrow indicates a triple point as observed in the TNM0.5C alloy

junctions of the same grain are tracked. These show a similar displacement behaviour, thus providing proof that the observation of triple point displacement actually reflects the motion of grain boundaries. In Fig. 4.15b) the displacements as a function of time of one triple point of the TNM and the molybdenum containing TN1.5Mo0.5C alloy are shown. The displacements are significantly smaller. It shall be noted that the scale is different on the y-axis in Fig. 4.15a) and Fig. 4.15b). Additionally, a general kinetic law to describe the time dependence of the average grain radius, as
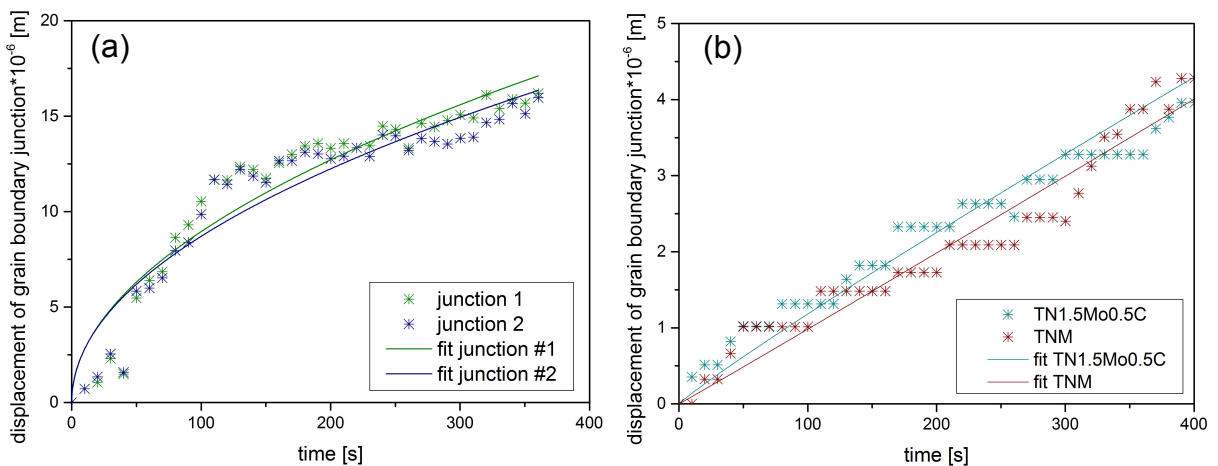

Fig. 4.15: Displacement of grain boundary junctions in a) the TNM0.5C alloy (for two different junctions) and b) the TNM alloy and the TN1.5Mo0.5C alloy.

given in Eq. 2.1, was fitted to the data points [24]. In Table 4.3 fitting parameters of this equation are given. The grain growth exponent n is close to 2 in the TNM0.5C alloy. This is attributed to grain boundary control of grain growth in pure single phase systems [24], which is in agreement of the fact that single α-phase is present at this temperature. In this case only the curvature of the grain boundary contributes to the driving force of grain boundary motion [26]. Reasons for deviations from the ideal value of 2 can be the presence of solute atoms. However, in the case of impurity drag deviations are comparably small [24].

In both the TNM alloy and the TN1.5Mo0.5C alloy two phases are present at 1300°C. Grain growth exponents are found to be close to 1. This value is attributed with the dissolution of a second phase [24]. This mechanism is likely, as in Fig. 4.14a) and Fig. 4.14b) remaining β-phase is visible, which aligns along the α grain boundaries.

Table 4.3: Fitting parameters gained from the datasets in Fig. 4.15. K is a constant, n is the grain growth exponent and R is the correlation coefficient.

alloy	K [μm^n/s]	n	R
TNM0.5C	0.816	2.034	0.95
	0.768	1.980	0.95
TNM	0.010	0.986	0.97
TN1.5Mo0.5C	0.012	1.074	0.99

The constant K includes the grain boundary energy as discussed in 2.1.3 and thus a measure of the driving force for boundary motion. The grain boundary energy differs for each grain boundary as it is dependent on the misorientation angle. Details can be found in [24,25]. Therefore, the chosen approach is only suitable for the determination of the time dependence but not for quantification of the grain size with respect to time. The constant K thus gives an indication of the growth rate. Large values correspond to high growth rates, small values correspond to slow growth. Thus, as expected, the TNM0.5C alloy, which shows a single phase α microstructure at 1300°C, shows significantly higher values for this parameter. This indicates that grain growth occurs on a different time scale in the TNM0.5C alloy.

Additionally, the correlation coefficient R was determined for each data set and is given in Table 4.3. Values in excess of 0.95 were obtained for all fitted data sets and hence, the applied law correlates in a highly significant manner to the data.

Following heat treatment in the infrared furnace of the HTLSCM the samples were prepared for the FEG-SEM. TNM and TN1.5Mo0.5C alloys did not show significant differences in microstructure compared to the initial state, whereas the microstructure of the TNM0.5C alloy changed significantly. In Fig. 4.16a) a SEM micrograph of the TNM0.5C alloy is displayed. Former grain boundaries of the α-phase (drawn in red dashed lines) are visible due to changes in orientation of the γ-lamellae. The grain

size is large in the range of a few hundred micrometres, which qualitatively confirms the *in-situ* observations previously described. Additional features of the microstructure are marked. The blue arrow points at a small amount of β-phase, either originating from sluggish dissolution behaviour or from secondary precipitation during cooling. The red arrow indicates borides, which were identified using EDX analysis. These elongated precipitates were found to be enriched with niobium (in agreement with [30]).

One observation additionally underlines the advantage of the absence of an α single phase field region. In the TN1.5Mo0.5C alloy a site was detected in the SEM after the annealing procedure as shown in Fig. 4.16b), where very little β-phase is present. The reason for that can be the inhomogeneous distribution of refractory metals in the
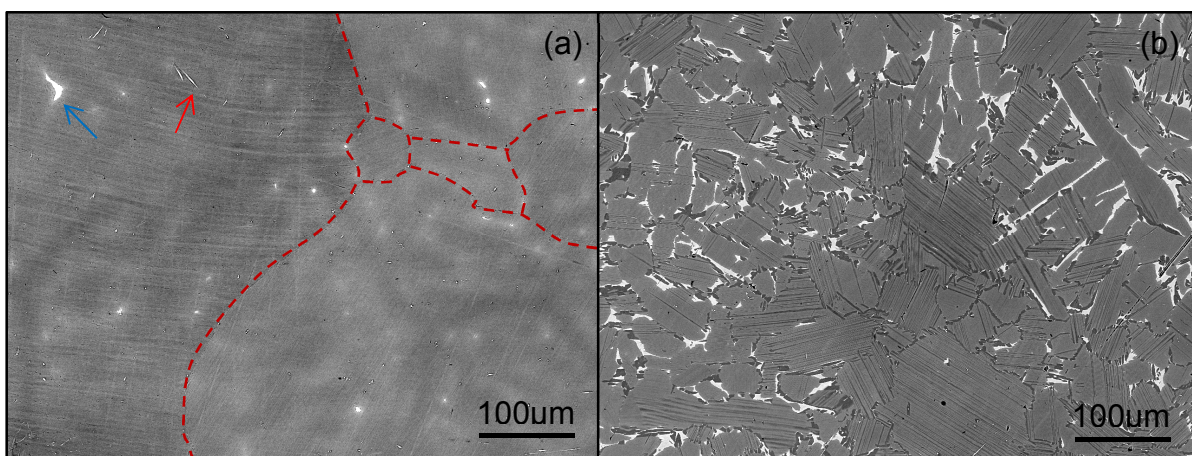

Fig. 4.16: a) FEG-SEM micrograph of a TNM0.5C sample heat treated at 1300°C for 20min. Dashed red line marks the former grain boundaries of the α-phase. Blue arrow indicates β-phase; red arrow indicates borides. b) FEG-SEM micrograph of a TN1.5Mo0.5C sample heat treated at 1300°C for 20min. A region with less β-phase where significant grain coarsening occurred is visible. The images were taken in BSE mode.

alloy. Moreover, in this region very coarse α_2/γ-colonies are present, which means that significant grain growth occurred in this region of the sample. This shows that chemical inhomogeneities can deteriorate the refined microstructure, which can be retained during high temperature heat treatments if sufficient β-phase is present along the grain boundaries.

In conclusion it can be said that one of the positive features of the TNM alloy is its very stable microstructure even at very high temperatures, whereas other TiAl based alloys are prone to grain growth [49].

4.5 Grain growth in the β single phase field region

In the processing of TiAl alloys especially β-solidifying alloys are of interest due to their good mechanical properties. On cooling after solidification an alloy has to go through the β single phase field region at least once and the risk is that the material will undergo grain growth while it is within this field. The materials under investigation are the TNM alloy and the TN1.5Mo0.5C alloy, because the TNM0.5C alloy does not

show a β single phase field region. In the following an approach to employ the HTLSCM to determine the grain size as a function of time will be discussed.

Grain growth was studied at annealing temperatures (T_A) within the β single phase field region, at 1405°C and at 1475°C for the TNM alloy and the TN1.5Mo0.5C alloy, respectively. Both alloys were heated to the given temperature at a heating rate of 1.67°C/s and were subsequently isothermally annealed in the infrared furnace of the HTLSCM. After the experiment the specimens were cooled at a rate of 1.67°C/s to room temperature. In order to obtain statistically reliable data, the grain size of a large number of grains was determined. The evolution of at least 20 grains was followed by utilizing this approach. Hence, a region around the sample centre of about 2mm side length was mapped in time intervals. Subsequently these images were superimposed using Paint.NET software. Thereafter the grain size was determined firstly by applying the mean linear intercept method. This method utilizes a grid of lines, which is superimposed on the image of interest. Thereafter intercepts of these lines with the grain boundaries are counted and divided by the overall line length. The inverse of this number corresponds to the grain size and is called the mean linear intercept [51]. Secondly, thresholding of the maps was carried out by using ImageJ® software. With this approach it is possible to manually measure the perimeter of grains. Thereafter the so-called mean equivalent circle diameter can be calculated. It has to be stated that both methods give valid results only, if the grain structure is equiaxed. To illustrate the measurement technique an example of a superimposed image of the grain structure in the TNM alloy after 12.5min is displayed in Fig. 4.17a). Fig. 4.17b) shows the corresponding image after thresholding was performed. Significant surface roughening due to previous phase transformations and dissimilar thermal expansion of the phases are visible. However, the grain boundaries can be clearly distinguished. The grain in the left upper corner is significantly larger than the others in this image, but the grain size is generally in the range of a few hundred micrometres. Additionally, the grain boundary shows a wavy structure. This illustrates that the movement of grain boundaries does not start at the same time for all grains. Moreover, the movement of single grain boundaries is often not uniform, because pinning can occur which leads to the waviness of the grain boundary. Interaction as observed is interpreted to be due to interaction with particles such as titanium borides. In addition, a grain boundary can be pinned by the thermal groove itself [25]. Within these experiments it was often observed that boundary motion only starts after a distinct time. As assumed previously this could be an effect of pinning by thermal grooves. A problem to be considered is that after a grain boundary moved on, the thermal groove is still visible for a while. Only through experience is it possible to distinguish between a remaining thermal groove and an actual grain boundary. This problem leads to the difficulty of evaluating the generated maps auto-

matically using image analysing software. The grain sizes determined by the techniques outlined above were plotted as a function of time for both the TNM and
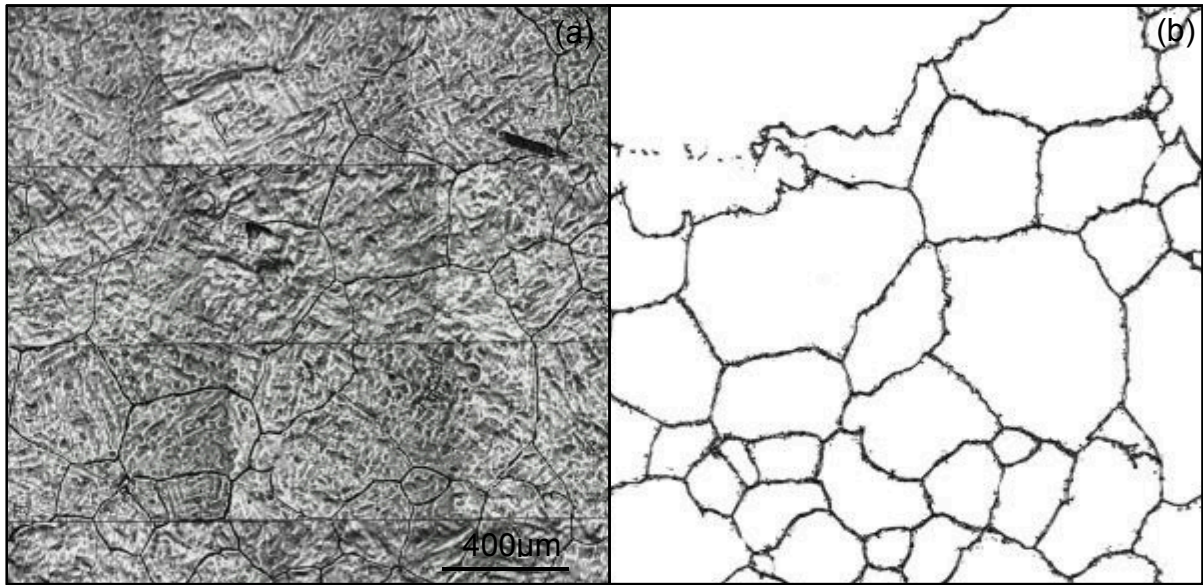

Fig. 4.17: a) Superimposed image of the sample centre of the TNM alloy after 12.5min at 1405°C; b) corresponding image after thresholding was performed.

the TN1.5Mo0.5C alloy. Fig. 4.18a) shows the development of the grain size in the TNM alloy at 1405°C, while Fig. 4.18b) shows the change in grain size in the TN1.5Mo0.5C alloy at 1475°C. Both measures of grain size, mean linear intercept and mean equivalent circle, are displayed. It has to be remarked that both time and grain size are scaled differently in Fig. 4.18a) and b). Both utilized methods give similar values for the grain size. Annealing the TNM alloy at 1405°C for 7min does not influence the grain size significantly. The treatment of the TN1.5Mo0.5C alloy for the same time at 1475°C leads to grains that doubled in diameter.
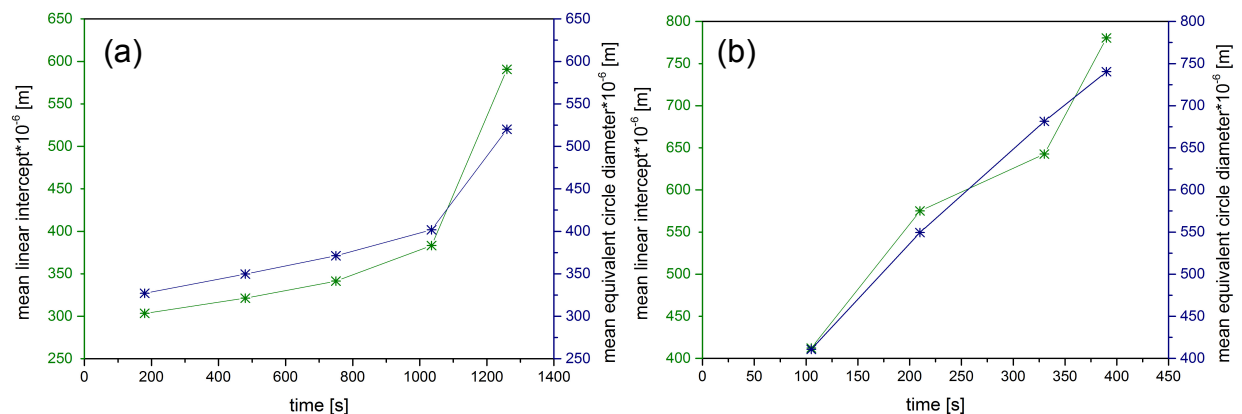
Fig. 4.18: Evolution of the grain size in a) TNM alloy at T_A=1405°C and b) TN1.5Mo0.5C alloy at T_A=1475°C.

In conclusion, it can be remarked, that passing through the β-phase field region on cooling is less 'dangerous' for the TNM alloy because grain coarsening occurs on a different time scale, whereas particular care has to be taken to pass through this phase field region in the TN1.5Mo0.5C alloy.

5 SUMMARY AND CONCLUSION

Solid-state phase transformations and grain growth were investigated in the TNM alloy, the TNM0.5C alloy and the TN1.5Mo0.5C alloy using a high temperature laser scanning confocal microscope (HTLSCM). By this technique *in-situ* observations can be made in real time of events that occur at high temperature under a protective atmosphere. Temperature calibration was done by using the nucleation of δ-ferrite in a low-carbon steel.

The image in the HTLSCM is generated by scanning the surface with a laser beam continuously and contrast is obtained mainly through thermal etching. The technique yields video sequences of the processes under investigation. Supporting FEG-SEM investigations were conducted at room temperature.

Part I: Solid-state phase transformation

The formation of the α-phase was investigated in the TNM alloy and the TN1.5Mo0.5C alloy. After annealing in the β single phase field region the samples were cooled at different rates. The morphology of the α-phase was found to be highly dependent on the cooling rate. At low cooling rates planar interfaces dominate the morphological evolution. At high cooling rates Widmanstätten laths, similar to morphological structures in titanium alloys, dominate the morphological evolution. After the cooling period the phase fraction of the α-phase was determined. Low cooling rates yielded large amounts of α-phase, whereas high cooling rates yielded small amounts of α-phase. This emphasizes a strong phase non-equilibrium phase evolution at high cooling rates, which leads to a partial suppression of the α-formation and an excess of the β-phase. This data can for example be utilized for the enhancement of industrial heat treatments as certain mechanical properties such as ductility and fracture toughness are dependent on the morphology of the previously evolving α-phase.

Both Widmanstätten laths and planar growth occur at intermediate cooling rates. However, the onset temperature of the growth of Widmanstätten laths is higher. Yet, it cannot be ruled out that this finding is due to the surface sensitive imaging principle of the HTLSCM.

No significant modifications of the β → α phase transformation were found that could be attributed to an alloying effect.

Further research such as partly transforming the microstructure via heat treatment into the α-phase, subsequent quenching and investigation of the interfaces using transmission electron microscopy (TEM) is necessary to extend the understanding of morphological evolution. Different types of interfaces are expected at planar growth

fronts and at Widmanstätten type laths. Additionally, the dependence of orientation relationships between β- and α-phase on the cooling rate is of interest as suggested in [9]. These can be elucidated using electron backscatter diffraction (EBSD).

In the carbon containing TN1.5Mo0.5C alloy the precipitation of a second phase was observed while annealing in the β single phase field region. These precipitates were identified as Ti_2AlC carbides by using EDX analysis. The observed carbides are of hexagonal structure, and are hence denoted as H-phase. The formation and growth of these carbides are due to the limited solubility of carbon in the β-phase, which provokes separation and precipitation. However, due to their large size this type of carbides is not useful in regard of precipitation hardening.

CCT diagrams were derived for the onset of phase transformation from the captured data of the β → α phase transformation. The highest undercooling for the onset of phase transformation in the TNM alloy and the TN1.5Mo0.5C alloy was determined to be 46°C and 31°C, respectively. A possibility to assess the validity of the CCT diagrams determined in this study would be a comparison with diagrams determined by dilatometry or DSC experiments.

The formation of the γ-phase was investigated in the TNM alloy, the TNM0.5C alloy and the TN1.5Mo0.5C alloy following cooling to below the α-transus temperature. The time until the onset of transformation was shortest for the TNM alloy and longest for the TN1.5Mo0.5C alloy.

The influence of carbon additions to the basic alloy on the interlamellar spacing was qualitatively shown. The interlamellar spacing is significantly smaller in carbon containing alloys, which contributes to the high strength of carbon containing TiAl alloys. However, these studies should be extended by high resolution methods as the size of the γ-lamellae is smaller than the resolution limit of the HTLSCM.

TNM samples were annealed at 1290°C and thereafter quenched in water. This procedure leads to a supersaturated microstructure due to the suppression of the formation of γ-phase. These samples were subsequently annealed below the eutectoid temperature and a cellular reaction was detected. The occurrence of this cellular reaction was proven by using FEG-SEM analysis. In TNM alloys the cellular reaction is associated with an increase of ductility due to a refinement of the microstructure.

Part II: Grain boundary motion and grain growth

Grain boundary displacement was studied in the TNM alloy, the TNM0.5C alloy and the TN1.5Mo0.5C alloy at 1300°C. In the TNM alloy and the TN1.5Mo0.5C alloy the displacement was small, which is attributed to the presence of an α+β phase field region at this temperature. The β-phase aligns along α grain boundaries, which

reduces their mobility. The dissolution of the β-phase is very slow, because it is stabilized by the slowly diffusing refractory metals. The occurrence of the β-phase yields a stable microstructure in this temperature regime, which is conducive to effective heat treatments and forging. The α single phase field region in the TNM0.5C alloy leads to an unstable microstructure. The grain boundaries are very mobile, which leads to significant grain coarsening. Grain boundary motion follows a parabolic law with respect to time, which is attributed to the motion in a single phase microstructure. In the alloys containing two phases a linear relation of the displacement with respect to time was observed, which is attributed to the presence of a second phase.

Below the solidus temperature a β single phase field region occurs in the TNM alloy and the TN1.5Mo0.5C alloy. In this regime grain growth was studied by determining the grain size as a function of time. The grain size was determined using the mean linear intercept method and the mean equivalent circle method. In the TN1.5Mo0.5C alloy grain growth occurred faster than in the TNM alloy. The β single phase microstructure is found at higher temperatures in the carbon containing TN1.5Mo0.5C alloy, which is the reason for the high grain boundary mobility.

In order to avoid significant grain growth in an industrial process, such as casting, it is important to cool through the β single phase field region as quickly as possible. The TNM alloy is more resistant to grain growth and, hence, the risk of excessive grain growth during cooling is less in this alloy than in the TN1.5Mo0.5C alloy. The major reason for this behaviour is that the β single phase field region occurs at a lower temperature field in the TNM alloy than in the TN1.5Mo0.5C alloy. This fact yields a lower mobility of the grain boundaries and, thus, a lower grain coarsening rate.

6 REFERENCES

[1]   H. Clemens, S. Mayer, "Design, Processing, Microstructure, Properties, and Applications of Advanced Intermetallic TiAl Alloys", Advanced Engineering Materials 15 (2013), 191-215

[2]   K. Kothari, R. Radhakrishnan, N.M. Wereley, "Advances in gamma titanium aluminides and their manufacturing techniques", Progress in Aerospace Sciences 55 (2012), 1-16

[3]   H. Clemens, M. Schloffer, E. Schwaighofer, R. Werner, A. Gaitzenauer, B. Rashkova, T. Schmoelzer, R. Pippan, S. Mayer, "Advanced β-Solidifying Titanium Aluminides - Development Status and Perspectives", MRS Fall Meeting, Boston (2012), 3-16

[4]   H. Kestler, H. Clemens, "Production, Processing and Application of γ(TiAl)-Based Alloys", in *Titanium and Titanium Alloys*, WILEY-VCH, Weinheim (2003), 351-392

[5]   T. Schmoelzer, K.D. Liss, G.A. Zickler, I.J. Watson, L.M. Droessler, W. Wallgram, T. Buslaps, A. Studer, H. Clemens, "Phase fractions, transition and ordering temperatures in TiAl-Nb-Mo alloys: An in- and ex-situ study", Intermetallics 18 (2010), 1544-1552

[6]   C. Scheu, E. Stergar, M. Schober, L. Cha, H. Clemens, A. Bartels, F.P. Schimansky, A. Cerezo, "High carbon solubility in a γ-TiAl-based Ti–45Al–5Nb–0.5C alloy and its effect on hardening", Acta Materialia 57 (2009), 1504-1511

[7]   H. Gabrisch, A. Stark, F.-P. Schimansky, L. Wang, N. Schell, U. Lorenz, F. Pyczak, "Investigation of carbides in Ti–45Al–5Nb–xC alloys (0 ≤ x ≤ 1) by transmission electron microscopy and high energy-XRD", Intermetallics 33 (2013), 44-53

[8]   E. Schwaighofer, H. Clemens, S. Mayer, J. Lindemann, J. Klose, W. Smarsly, V. Güther, "Microstructural design and mechanical properties of a cast and heat-treated intermetallic multi-phase γ-TiAl-based alloy", Intermetallics 44 (2014), 128-140

[9]   M. Oehring, A. Stark, J.D.H. Paul, T. Lippmann, F. Pyczak, "Microstructural refinement of boron-containing β-solidifying γ-titanium aluminide alloys through heat treatments in the β phase field", Intermetallics 32 (2013), 12-20

[10]   D. Phelan, M. Reid, N. Stanford, R. Dippenaar, "In-Situ Observations of Phase Transformations in Titanium", JOM (2006), 67-69

[11]   H. Clemens, S. Mayer, "Intermetallic γ-Titanium aluminide based alloys from a metallographic point of view - A continuation", Practical Metallography 48 (2011), 64-100

[12]   M. Peters, J. Hemptenmacher, J. Kumpfert, C. Leyens, "Structure and Properties of Titanium and Titanium Alloys", in *Titanium and Titanium Alloys*, WILEY-VCH, Weinheim (2003), 1-36

[13]   F. Appel, M. Oehring, "γ-Titanium Aluminide Alloys: Alloy Design and Properties", in *Titanium and Titanium Alloys*, WILEY-VCH, Weinheim (2003), 89-152

[14]   W. Wallgram, T. Schmoelzer, L. Cha, G. Das, V. Güther, H. Clemens, "Technology and mechanical properties of advanced γ-TiAl based alloys", Int. J. Mat. Res. 100 (2009), 1-10

[15]   M. Takeyama, S. Kobayashi, "Physical metallurgy for wrought gamma titanium aluminides: Microstructure control through phase transformations", Intermetallics 13 (2005), 993-999

[16] H. Clemens, W. Wallgram, S. Kremmer, V. Güther, A. Otto, A. Bartels, "Design of Novel β-Solidifying TiAl Alloys with Adjustable β/B2-Phase Fraction and Excellent Hot-Workability", Advanced Engineering Materials 10 (2008), 707-713

[17] A. Stark, M. Oehring, F. Pyczak, A. Schreyer, "In Situ Observation of Various Phase Transformation Paths in Nb-Rich TiAl Alloys during Quenching with Different Rates", Advanced Engineering Materials 13 (2011), 700-704

[18] U. Hecht, V. Witusiewicz, A. Drevermann, J. Zollinger, "Grain refinement by low boron additions in niobium-rich TiAl-based alloys", Intermetallics 16 (2008), 969-978

[19] J.A. Christodoulou, H.M. Flower, "The Role of Borides in Near-γ Titanium Aluminides", Advanced Engineering Materials 2 (2000), 631-638

[20] R.M. Imayev, V.M. Imayev, M. Oehring, F. Appel, "Alloy design concepts for refined gamma titanium aluminide based alloys", Intermetallics 15 (2007), 451-460

[21] W. Kurz, D.J. Fisher, "Fundamentals of solidification ", CRC Press, Boca Raton (1998)

[22] D.A. Porter, K.E. Easterling, M.Y. Sherif, "Phase Transformations in Metals and Alloys", CRC Press, Boca Raton (2009)

[23] V. Küstner, "Untersuchungen zur Gefügebildung bei der Erstarrung von γ-Titanaluminid-Legierungen unterschiedlicher Konstitution", Christian-Albrechts Universität zu Kiel (2003)

[24] H.V. Atkinson, "Overview no. 65: Theories of normal grain growth in pure single phase systems", Acta Metallurgica 36 (1988), 469-491

[25] G. Gottstein, L.S. Shvindlerman, "Grain Boundary Migration in Metals - Thermodynamics, Kinetics, Applications", CRC Press, Boca Raton (2010)

[26] J. Burke, D. Turnbull, "Recrystallization and grain growth", Progress in Metal Physics 3 (1952), 220-292

[27] H.I. Aaronson, M. Enomoto, J.K. Lee, "Mechanisms of Diffusional Phase Transformations in Metals and Alloys", CRC Press, Boca Raton (2010)

[28] Y. Wang, Y. Liu, G. Yang, H. Li, B. Tang, "Microstructure of cast γ-TiAl based alloy solidified from the β phase region", Trans. Nonferrous. Met. Soc. China 21 (2011), 215-222

[29] W.G. Burgers, "On the process of transition of the cubic-body-centered modification into the hexagonal-close-packed modification of zirconium", Physica 1 (1934), 561-586

[30] H. Clemens, H.F. Chladil, W. Wallgram, G.A. Zickler, R. Gerling, K.-D. Liss, S. Kremmer, V. Güther, W. Smarsly, "In and ex situ investigations of the β-phase in a Nb and Mo containing γ-TiAl based alloy", Intermetallics 16 (2008), 827-833

[31] R. Schnitzer, H.F. Chladil, C. Scheu, H. Clemens, S. Bystrzanowski, A. Bartels, S. Kremmer, "The Production of Lamellar Microstructures in Intermetallic TiAl Alloys and their Characterisation", Practical Metallography 44 (2007), 430-442

[32] M. Blackburn, in *The Science, Technology and Application of Titanium*, Pergamon Press Ltd., Oxford (1970), 633-643

[33] R.V. Ramanujan, "Phase transformations in γ based titanium aluminides", International Materials Reviews 45 (2000), 217-240

[34] D. Hu, A.J. Huang, X. Wu, "On the massive phase transformation regime in TiAl alloys: The alloying effect on massive/lamellar competition", Intermetallics 15 (2007), 327-332

[35] E. Schwaighofer, M. Schloffer, T. Schmoelzer, S. Mayer, J. Lindemann, V. Güther, J. Klose, H. Clemens, "Influence of Heat Treatments on the Microstructure of a Multi-Phase Titanium Aluminide Alloy", Practical Metallography 49 (2012), 124-137

[36] L.M. Droessler, T. Schmoelzer, W. Wallgram, L. Cha, G. Das, H. Clemens, "Microstructure and Tensile Ductility of a Ti-43Al-4Nb-1Mo-0.1B Alloy", Mater. Res. Soc. Symp. Proc., Warrendale (2009), 121-126

[37] L. Cha, C. Scheu, H. Clemens, H.F. Chladil, G. Dehm, R. Gerling, A. Bartels, "Nanometer-scaled lamellar microstructures in Ti-45Al-7.5Nb-(0; 0.5)C alloys and their influence on hardness", Intermetallics 16 (2008), 868-875

[38] I. Manna, S.K. Pabi, W. Gust, "Discontinuous reactions in solids", International Materials Reviews 46 (2001), 53-91

[39] L. Cha, H. Clemens, G. Dehm, "Microstructure evolution and mechanical properties of an intermetallic Ti-43.5-4Nb-1Mo-0.1B alloy after ageing below the eutectoid temperature", Int. J. Mat. Res. 102 (2011), 703-708

[40] M. Schloffer, F. Iqbal, H. Gabrisch, E. Schwaighofer, F.P. Schimansky, S. Mayer, A. Stark, T. Lippmann, M. Göken, F. Pyczak, H. Clemens, "Microstructure development and hardness of a powder metallurgical multi phase γ-TiAl based alloy", Intermetallics 22 (2012), 231-240

[41] W.H. Tian, M. Nemoto, "Effect of carbon addition on the microstructures and mechanical properties of γ-TiAl alloys", Intermetallics 5 (1997), 237-244

[42] Y. Wu, Y.W. Park, H.S. Park, S.K. Hwang, "Microstructural development of indirect-extruded TiAl-Mn-Mo-C intermetallic alloys during aging", Materials Science and Engineering A347 (2003), 171-179

[43] S.F. Matar, Y.L. Petitcorps, J. Etourneau, "Local density functional calculations of the electronic structures of Ti_2AlC and Ti_3AlC", J. Mater. Chem. 7 (1997), 99-103

[44] E. Schwaighofer, B. Rashkova, H. Clemens, A. Stark, S. Mayer, "Effect of carbon addition on solidification behavior, phase evolution and creep properties of an intermetallic β-stabilized γ-TiAl based alloy", Intermetallics (2013), submitted

[45] M. Minski, "Microscopy Apparatus", US Patent (1961), 3,013,467

[46] W.W. Mullins, "Theory of Thermal Grooving", J. Appl. Phys. 28 (1957), 333-339

[47] D. Phelan, "In-Situ Studies of phase transformations in iron alloys", Dissertation, University of Wollongong (2002)

[48] D. Phelan, M. Reid, R. Dippenaar, "High Temperature Laser Scanning Confocal Microscopy for real-time studies of phase transformations", Micrsoscopy and Microanalysis 11 (2005), 670-671

[49] I.J. Watson, K.-D. Liss, H. Clemens, W. Wallgram, T. Schmoelzer, T.C. Hansen, M. Reid, "In Situ Characterisation of a Nb and Mo Containing γ-TiAl Based Alloy Using Neutron Diffraction and High-Temperature Microscopy", Advanced Engineering Materials 11 (2009), 932-937

[50] H.S. Park, S.W. Nam, N.J. Kim, S.K. Hwang, "Refinement of the lamellar structure in TiAl-BASED intermetallic compound by addition of carbon", Scripta Materialia 41 (1999), 1197-1203

[51] B. Roebuck, "Measurement of grain size and size distribution in engineering materials", Materials Science and Technology 16 (2000), 1167-1174

7 APPENDIX

A CD of selected transformation sequences is enclosed at the end of this thesis.

β → α phase transformation

Table 7.1 summarizes the enclosed video files on the β → α phase transformation. Discussion of cooling rate and alloying influence can be found in subchapter 4.2.2.

Table 7.1: Cooling rates, start temperature (T_1), end temperature (T_2) and name on CD for the β → α phase transformation.

alloy	cooling rate [°C/s]	T_1 [°C]	T_2 [°C]	name on CD
TNM	0.03	1405	1325	A
	12.0	1405	1325	B
	1.00	1405	1325	C
TN1.5Mo0.5C	0.03	1475	1395	D
	11.54	1475	1395	E
	1.00	1475	1395	F

γ-formation

Table 7.2 summarizes the enclosed video files on the γ-formation. Discussion of alloying influence can be found in subchapter 4.3.1.

Table 7.2: Cooling rate, start temperature (T_1), end temperature (T_2) and name on CD for the γ-formation.

alloy	cooling rate [°C/s]	T_1 [°C]	T_2 [°C]	name on CD
TNM	12.50	1300	1150	G
TN1.5Mo0.5C	12.50	1300	1150	H
TNM0.5C	12.50	1300	1150	I